Article

Neuron

Rapid Reconfiguration of the Functional Connectome after Chemogenetic *Locus Coeruleus* Activation

Graphical Abstract

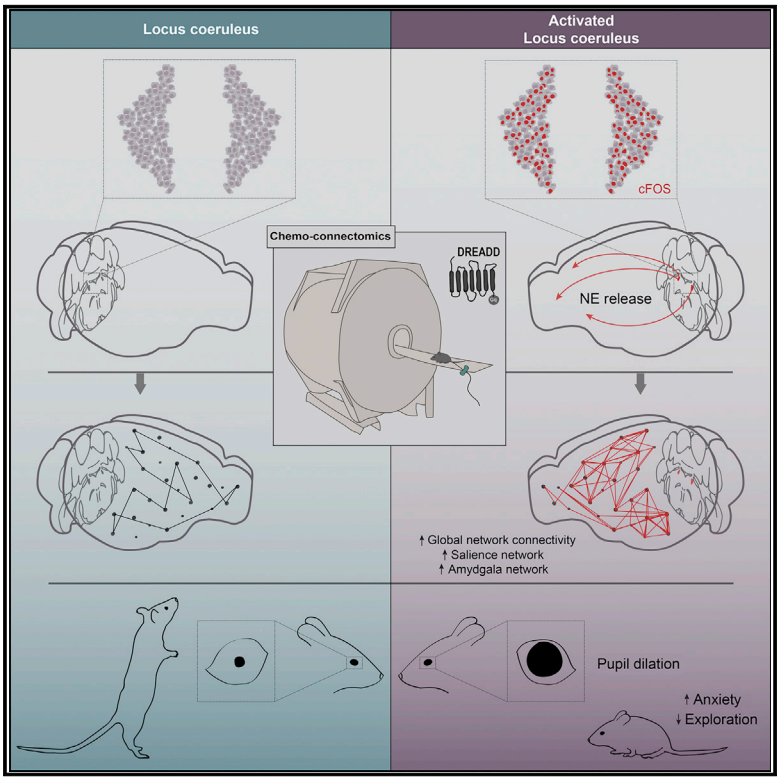

Highlights

- Chemo-connectomics combines chemogenetics (DREADDs) with resting-state fMRI
- *Locus coeruleus* (LC) activation rapidly increases brain-wide functional connectivity
- Connectivity changes correlate positively with adrenergic receptor distribution
- LC activation shifts large-scale network connectivity toward salience processing

Authors

Valerio Zerbi, Amalia Floriou-Servou, Marija Markicevic, ..., Peter Paul De Deyn, Nicole Wenderoth, Johannes Bohacek

Correspondence

valerio.zerbi@hest.ethz.ch (V.Z.), nicole.wenderoth@hest.ethz.ch (N.W.), johannes.bohacek@hest.ethz.ch (J.B.)

In Brief

Zerbi et al. selectively activate the mouse *locus coeruleus*, which provides norepinephrine to the brain. This induces anxiety and rapidly shifts network connectivity toward salience and fear processing. This appears to be mediated by the spatial distribution of adrenergic receptors.

Zerbi et al., 2019, Neuron *103*, 702–718
August 21, 2019
https://doi.org/10.1016/j.neuron.2019.05.034

CellPress

CellPress

Neuron
Article

Rapid Reconfiguration of the Functional Connectome after Chemogenetic *Locus Coeruleus* Activation

Valerio Zerbi,[1,7,8,*] Amalia Floriou-Servou,[2,7,8] Marija Markicevic,[1,7] Yannick Vermeiren,[3,5] Oliver Sturman,[2,7] Mattia Privitera,[2,7] Lukas von Ziegler,[2,7] Kim David Ferrari,[4,7] Bruno Weber,[4,7] Peter Paul De Deyn,[3,5,6] Nicole Wenderoth,[1,7,*] and Johannes Bohacek[2,7,9,*]

[1]Neural Control of Movement Lab, Department of Health Sciences and Technology, ETH Zürich, Zürich, Switzerland
[2]Laboratory of Molecular and Behavioral Neuroscience, Institute for Neuroscience, Department of Health Sciences and Technology, ETH Zürich, Zürich, Switzerland
[3]Laboratory of Neurochemistry and Behavior, Institute Born-Bunge, Department of Biomedical Sciences, University of Antwerp, Wilrijk (Antwerp), Belgium
[4]Experimental Imaging and Neuroenergetics, Institute of Pharmacology and Toxicology, University of Zürich, Zürich, Switzerland
[5]Department of Neurology and Alzheimer Center, University of Groningen and University Medical Center Groningen (UMCG), Groningen, the Netherlands
[6]Department of Neurology, Memory Clinic of Hospital Network Antwerp (ZNA) Middelheim and Hoge Beuken, Antwerp, Belgium
[7]Neuroscience Center Zürich, ETH Zürich and University of Zürich, Zürich, Switzerland
[8]These authors contributed equally
[9]Lead Contact
*Correspondence: valerio.zerbi@hest.ethz.ch (V.Z.), nicole.wenderoth@hest.ethz.ch (N.W.), johannes.bohacek@hest.ethz.ch (J.B.)
https://doi.org/10.1016/j.neuron.2019.05.034

SUMMARY

The *locus coeruleus* (LC) supplies norepinephrine (NE) to the entire forebrain and regulates many fundamental brain functions. Studies in humans have suggested that strong LC activation might shift network connectivity to favor salience processing. To causally test this hypothesis, we use a mouse model to study the effect of LC stimulation on large-scale functional connectivity by combining chemogenetic activation of the LC with resting-state fMRI, an approach we term "chemo-connectomics." We show that LC activation rapidly interrupts ongoing behavior and strongly increases brain-wide connectivity, with the most profound effects in the salience and amygdala networks. Functional connectivity changes strongly correlate with transcript levels of alpha-1 and beta-1 adrenergic receptors across the brain, and functional network connectivity correlates with NE turnover within select brain regions. We propose that these changes in large-scale network connectivity are critical for optimizing neural processing in the context of increased vigilance and threat detection.

INTRODUCTION

The *locus coeruleus* (LC) is a small structure in the brain stem (with approximately 1,500 neurons in each hemisphere in mice and 20,000 in humans) (Manaye et al., 1995; Sara and Bouret, 2012) that sends widespread efferent projections to almost the entire brain and constitutes the major source of norepinephrine (NE) to most forebrain regions. Dysregulation of the LC-NE system has been implicated in numerous psychiatric pathologies, including depression, anxiety, attention deficit hyperactivity disorder, post-traumatic stress disorder, and neurodegenerative diseases (Bangasser et al., 2019; Fortress et al., 2015; Isingrini et al., 2016; Weinshenker, 2018). The ability to selectively change activity within the LC-NE system with optogenetics and chemogenetics has confirmed that the LC has a strong modulatory effect on various functional circuits related to wakefulness (Carter et al., 2010) and cognitive function (Uematsu et al., 2017; Usher et al., 1999) and on stress-related behavioral responses, including fear, anxiety, and avoidance (Hirschberg et al., 2017; McCall et al., 2015, 2017). These widespread effects are in line with theories that the LC optimizes cognitive processes relevant for task performance or adaptive behaviors by rearranging neural activity within and between large-scale neuronal systems (Aston-Jones and Cohen, 2005; Bullmore and Sporns, 2009; van den Heuvel and Hulshoff Pol, 2010; Seeley et al., 2007).

Phasic LC activation, as triggered by salient stimuli, enhances cognitive performance and facilitates faster orientation toward task-relevant cues (Aston-Jones and Cohen, 2005; Berridge and Waterhouse, 2003). In contrast, high tonic LC activity, as reliably triggered by various stressors, causes the release of substantial quantities of NE throughout the brain (Arnsten, 2009; Valentino and Van Bockstaele, 2008), which is thought to have a "circuit breaker" function that allows interruption of ongoing neural activity and rapid reconfiguration of functional communication between brain regions (i.e., functional networks) (Arnsten, 2009; Corbetta et al., 2008). This rapid response is evolutionarily conserved because it benefits survival by enabling the selection of adaptive behaviors in threatening situations (Roeder, 2005). However, it has not been demonstrated directly that increased LC activity reconfigures functional neural networks across the brain, and it remains unknown how the widespread LC projections might achieve specificity for regulating specific networks.

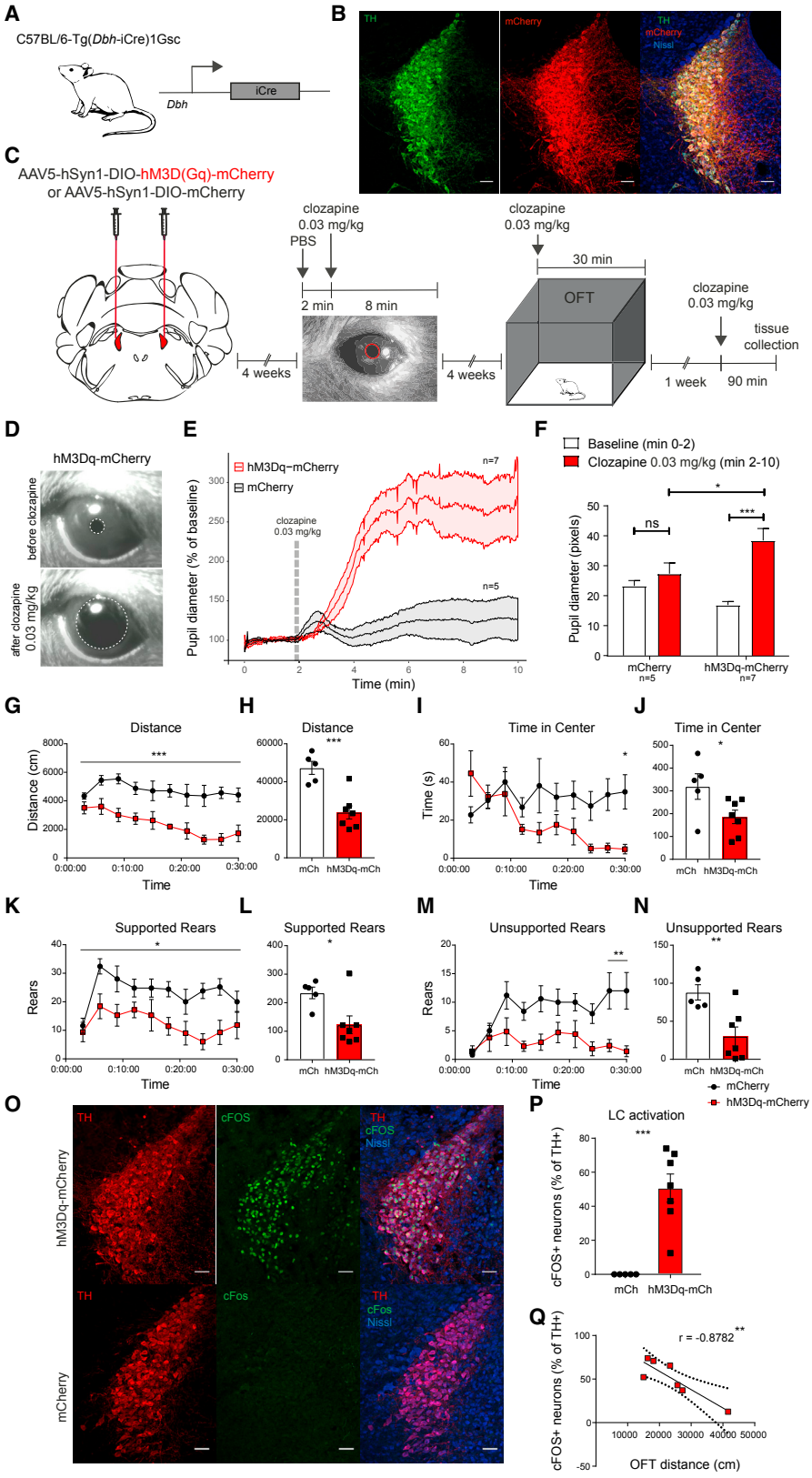

(legend on next page)

Some evidence suggests that strong LC activation by environmental cues, as observed during acutely stressful situations, plays an important role in activating networks that favor salience processing and action selection (Aston-Jones and Cohen, 2005; Hermans et al., 2014) and that regional specificity is achieved through the distribution of adrenergic receptors (Arnsten, 2009). In humans, acute stress exposure dynamically shifts large-scale network activity toward higher activation of the salience network, including the amygdala (van Marle et al., 2010), which is mediated by beta adrenergic receptors (Hermans et al., 2011), promoting hypervigilance and threat detection at the cost of executive control (Corbetta et al., 2008; Hermans et al., 2014). However, direct involvement of the LC has not been proven because it is impossible to selectively manipulate LC activity in humans.

To explore whether LC activation changes local and global network organization, we used a mouse model and applied a novel "chemo-connectomics" approach, which combines (1) cell-specific chemogenetic manipulation of neural activity afforded by designer receptors exclusively activated by designer drugs (DREADDs) (Armbruster et al., 2007) with (2) a brain-wide functional connectome analysis as revealed by resting-state fMRI (rs-fMRI). This approach leverages the molecular tools and genome-wide resources available in mice and allows us to link functional connectivity (FC) with micro- and mesoscopic properties of the mouse brain. We asked (1) whether a selective increase in LC activity would change the FC profile of large-scale brain networks or connectomes, (2) whether such network-wide effects are related to the known distribution of adrenergic receptor subtypes across the brain, and (3) whether changes in FC correspond to the levels of NE release in the target structures.

RESULTS

To selectively target the LC, we used transgenic mice that express codon-improved Cre recombinase (iCre) under the dopamine-beta-hydroxylase (DBH) promoter (DBH-iCre mice; Figure 1A; Parlato et al., 2007). We stereotactically delivered floxed excitatory DREADDs (Roth, 2016) (AAV5-hSyn-DIO-hM3Dq-mCherry; hM3Dq-mCh) or a control virus (AAV5-hSyn-DIO-mCherry; mCh) to the LC, restricting virus expression to DBH-positive noradrenergic neurons of the LC (Figure 1B). We assessed successful LC activation using pupillometry (Liu et al., 2017; Murphy et al., 2014; Reimer et al., 2016). After 2 min of baseline recording under light isoflurane anesthesia, we activated LC neurons by administering the potent DREADD activator clozapine at an ultra-low dose (0.03 mg/kg intraperitoneally [i.p.]; Figure 1C; Gomez et al., 2017). Within a minute of clozapine injection, we observed a strong increase in pupil diameter in the hM3Dq-mCh group, whereas the pupil diameter of mCh mice did not change in response to clozapine injection and remained stable throughout the 10-min recording session (Figures 1D–1F). To show that our LC activation protocol is behaviorally relevant, we subjected mice to an open field test (OFT) immediately after clozapine injection and recorded their behavior for 30 min. In comparison to mCh mice, clozapine injection had profound effects on the behavior of hM3Dq-mCh mice. Several minutes after clozapine administration, hM3Dq-mCh mice showed strongly suppressed locomotor activity (Figures 1G and 1H), spent less time in the (more aversive) center of the open field (Figures 1I and 1J), and performed fewer activity-related supported rears (Figures 1K and 1L) and fewer exploratory unsupported rears (Figures 1M and 1N; Sturman et al., 2018). This is in line with previous findings that LC activation suppresses motor activity (Carter et al., 2010; Hirschberg et al., 2017) and increases anxiety (Hirschberg et al., 2017; Li et al., 2018; McCall et al., 2015). Because the LC is a highly sexually dimorphic structure, we assessed whether these findings hold true in female mice as well. We confirmed that, after clozapine administration, hM3Dq-mCh females also showed reduced locomotor activity in the OFT (Figures S1B and S1C), spent less time in the center (Figures S1D and S1E), and performed fewer supported (Figures S1F and S1G) and unsupported rears (Figures S1H and S1I). To better characterize the effects of LC activation on behavior, we also tested these females in the light-dark box (LDB) for 30 min immediately after clozapine injection (Figure S1A). Compared with mCh mice, hM3Dq-mCh mice spent much less time in the aversive light compartment of the box (Figures S1J and S1K) and more time in the dark compartment (Figures S1L and S1M). They also traveled a shorter distance (Figures S1N and S1O), shuttled fewer times between the light and the dark compartment (Figure S1P), and performed fewer rears (Figures S1Q and S1R). These results indicate reduced exploratory behavior and increased anxiety. Because the strong suppression of locomotor activity could also be due

Figure 1. Physiological, Behavioral, and Molecular Effects of LC Activation with hM3Dq

(A) Schematic of *DBH*-iCre mouse genetics.

(B) mCherry (mCh) co-localizes with tyrosine hydroxylase (TH) in the LC of DBH-iCre mice after stereotactic delivery of AAV5-Syn1-DIO-mCh.

(C) Diagram of the experimental design.

(D) Images showing the pupil size before and after administration of clozapine in a mouse expressing hM3Dq-mCh in the LC.

(E and F) Pupil size increased rapidly after clozapine administration (E), and this effect was only observed in hM3Dq-mCh mice (F) (interaction time × group: $F(1,10) = 9.60$, $p = 0.0113$, two-way ANOVA with Sidak *post hoc* tests).

(G–N) Immediately after clozapine injection, hM3Dq-mCh mice traveled a shorter distance than mCh control mice (G and H; main effect of group: $F(1,10) = 21.92$, $p = 0.0009$, two-way ANOVA), spent less time in the center (I and J; main effect of group $F(1,10) = 5.15$, $p = 0.0467$; interaction: $F(9,90) = 3.04$, $p = 0.0032$, two-way ANOVA with Sidak *post hoc* tests), and performed fewer supported rears (K and L; main effect of group: $F(1,10) = 7.24$, $p = 0.0227$) and fewer unsupported rears (M and N; main effect of group: $F(1,10) = 11.33$, $p = 0.0072$, interaction: $F(9,90) = 2.46$, $p = 0.0148$).

(O) Representative images of cFOS expression in TH+ neurons in the LC of hM3Dq-mCh or mCh mice 90 min after injection of clozapine.

(P) Quantification of cFOS expression showing increased neuronal activation in hM3Dq-mCh mice ($t(10) = 5.12$, $p = 0.0005$, unpaired t test).

(Q) cFOS expression in the LC correlates with distance traveled in the OFT in hM3Dq-mCh mice ($r(5) = -0.8782$, $p = 0.0093$).

hM3Dq-mCh, n = 7; mCh, n = 5. *$p < 0.05$, **$p < 0.01$, ***$p < 0.001$. Data represent mean ± SEM. Scale bars, 50 μm. See also Figure S1.

to locomotor impairment, we trained the same mice on the rotarod (day 1) and then tested them on two consecutive days without clozapine (day 2) or with clozapine (day 3; Figure S1A). Both during training and testing, hM3Dq-mCh mice performed similarly before and after clozapine injection (Figure S1S), with no significant difference between groups or across daily trials (Figures S1T and S1U). Thus, the strong suppression in locomotor activity after LC activation is likely due to an increase in anxiety and not due to any gross locomotor impairment.

To molecularly validate activation of LC neurons, we returned to the same male mice that were used for OFT testing, injected them again with clozapine, collected their brains 90 min later, and assessed the neural activity marker cFOS in the LC using immunohistochemistry. As expected, we observed a strong increase in cFOS expression restricted to tyrosine hydroxylase-positive (TH+) noradrenergic neurons of the LC in hM3Dq-mCh mice, whereas cFOS was virtually absent in mCh mice (Figures 1O and 1P). Because behavior testing and cFOS staining were performed in the same mice, we correlated the locomotor activity of hM3Dq-mCh mice with the number of cFOS-positive neurons in the LC. We found a strong negative correlation (Figure 1Q), showing that the strength of LC activation predicts the suppression in locomotion and exploration. Thus, our chemogenetic strategy specifically activates LC neurons and rapidly induces behavioral changes that last at least 30 min.

LC Activation Drives Rapid Increases in FC

We hypothesized that an increase in LC-NE activity would rapidly reconfigure large-scale brain networks, as reflected by the functional connectome. We therefore acquired rs-fMRI data before and after hM3Dq-induced LC activation in a continuous imaging session. We kept mice under light isoflurane anesthesia and recorded 15 min of baseline fMRI before activating hM3Dq with clozapine (0.03 mg/kg intravenously [i.v.]) (Markicevic et al., 2018). After the clozapine injection, we continued the fMRI recordings for 8 min (i.e., transitory period), followed by another 15 min when the LC is expected to be robustly activated (i.e., active period), leading to a total uninterrupted scan time of 38 min (Figure 2A). We limited the duration of the functional imaging session to reduce the accumulation of isoflurane over time, which might otherwise affect the local excitation-inhibition balance and neurovascular coupling (Aksenov et al., 2015).

We first tested whether the observed changes in whole-brain connectivity were time-locked to DREADD activation. FC, defined as the Pearson's correlation of blood-oxygen-level-dependent (BOLD) activity between two regions (for details, see STAR Methods), was measured between 165 brain regions (nodes) using the Allen common coordinate framework and over 38 non-overlapping time bins of 1 min each. For each time bin, FC is measured between each pair of regions (edges), normalized to the subject's baseline connectivity (i.e., averaged across the first 15 min), and the effect size is calculated using the standardized difference between the group means (Cohen's D, hM3Dq-mCh versus mCh). During the first 15 min (baseline), Cohen's D varied, on average, between −0.12 and +0.10 (average, −0.00; null-to-small effect) and did not demonstrate an appreciable spatial or temporal pattern. However, immediately after clozapine injection, the effect size rapidly and significantly increased for the remainder of the scan session, showing increased connectivity in hM3Dq mice relative to mCh controls (Figures 2B and 2C). Effect sizes range, on average, from +0.21 to +0.38 (moderate effect) and up to +3.2 for individual edges (very strong effect).

Increased FC Is Dependent on LC-NE Signaling

We next tested whether the DREADD-induced connectivity changes could be pharmacologically blocked by medetomidine, a selective agonist of the inhibitory alpha-2 adrenergic receptor, which suppresses LC firing and NE release (Jorm and Stamford, 1993; Lakhlani et al., 1997). After pre-treating mice with a bolus injection of medetomidine (0.05 mg/kg i.v.), medetomidine was also continuously infused at 0.1 mg/kg/h i.v. to keep its levels stable throughout the ensuing rs-fMRI session (Grandjean et al., 2014). After 15 min of baseline recording, clozapine was administered (Figure 2A). Across all edges, Cohen's D did not vary significantly over time, showing that medetomidine prevented DREADD-induced LC activation (Figures 2D and 2E).

To examine the effect of different anesthesia regimens on FC over time, we compared the effect size in mCh mice between both anesthesia conditions (i.e., 1% isoflurane versus 0.5% isoflurane + medetomidine). We found no significant differences between the two experimental conditions in the baseline and transient periods (Figure S2). However, Cohen's D was slightly increased in the active period, suggesting a reduction in connectivity across all edges in the isoflurane group. This is a well-known effect, most likely caused by the accumulation of isoflurane over time (Bukhari et al., 2018). The net effect was, however, null to small (average, +0.04; minimum, −0.04; maximum, +0.129) and about 7 times smaller than the DREADD-driven effect.

Spatial Reconfiguration of the Functional Connectome after LC Activation Reflects Transcript Levels of Adrenergic Receptors

Next we mapped the location of the connections that were altered following LC activation. To this end, we compared the connectome matrix obtained from the first 15 min of the scan (baseline period) with the last 15 min of the scan (after clozapine, "active period"). Analysis of the functional connectome after LC-NE activation revealed a large group of edges that display increased FC in hM3Dq-mCh animals compared with mCh animals after clozapine injection (218 edges, time × group interaction, non-parametric, randomized permutation testing, family-wise error (FWE) corrected with network-based statistics at $p < 0.05$) (Figure 3A). The spatial distribution of these hyper-connected edges is widespread and involves 64% of the 165 brain regions considered in the analysis (105 regions of interest [ROIs]) (Figure 3B), which is in line with the widespread afferent fibers originating from the LC (Aston-Jones, 2004; Schwarz and Luo, 2015).

The analyses presented above suggest that different brain areas show distinctive connectivity changes upon LC-NE stimulation. To investigate this hypothesis, we determined how LC activation changes the overall connectivity strength of a single brain area as quantified by the "node modulation index" (NMI). The NMI is a surrogate marker obtained by averaging the effect size of connectivity changes induced by LC-NE stimulation

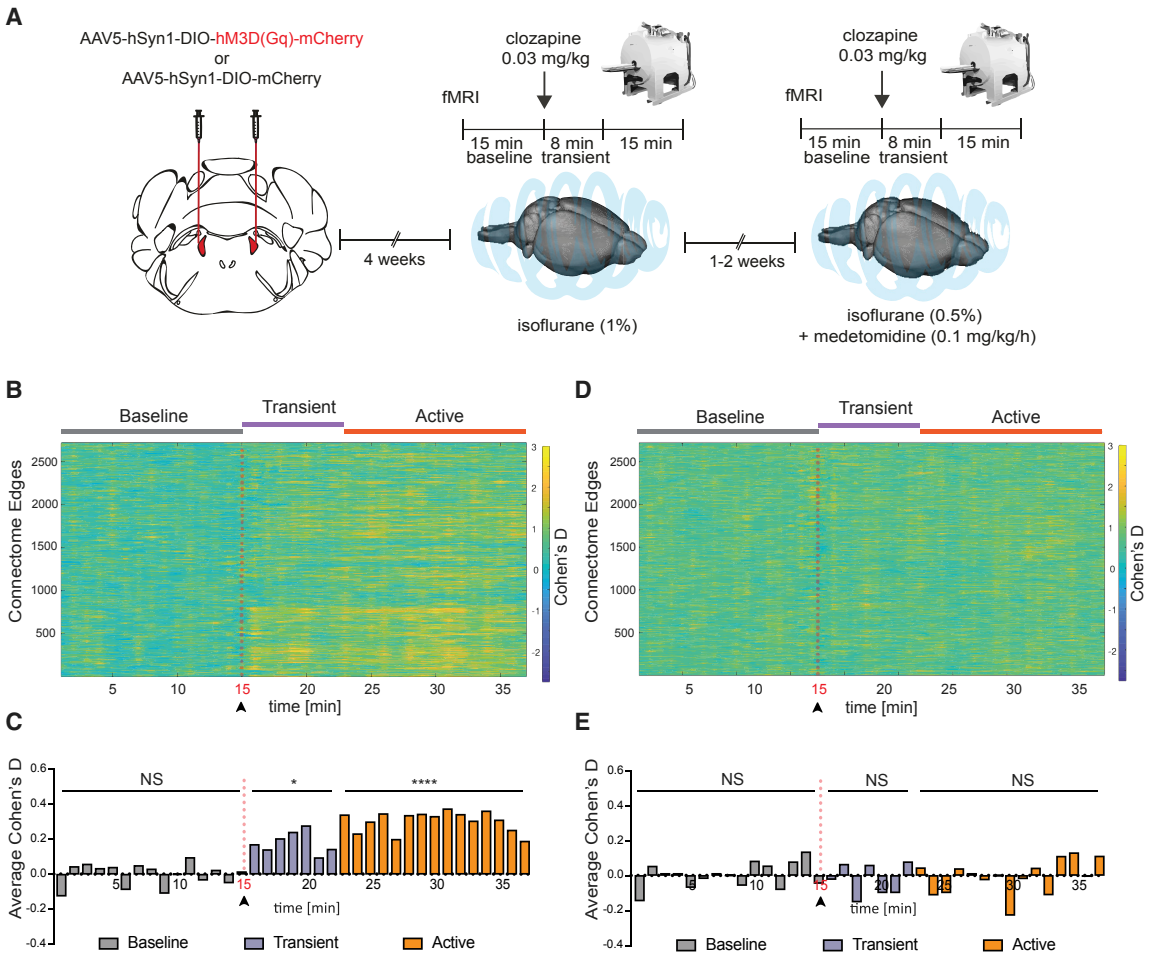

Figure 2. DREADD Activation of the LC Causes Time-Locked Changes in Functional Connectivity (FC)

(A) Schematic of the experimental setup for MRI recordings. 4 weeks after bilateral virus delivery, mice underwent two MRI sessions with the same experimental procedure but different anesthetic regimens.

(B–E) Effect size (Cohen's D) analysis of FC is shown for single edges (n = 2,724; B and D) and for the average across all edges (C and E). The data reveal time-locked increases in connectivity in multiple edges, starting immediately after clozapine (0.03 mg/kg) i.v. injection (Wilcoxon two-tailed test; $p = 0.804$ for the baseline period, $p = 0.015$ for the transient period, and $p < 0.0001$ for the active period).

(D and E) Treatment with the alpha-2 adrenergic agonist medetomidine (0.05 mg/kg + 0.1 mg/kg/h; STAR Methods) abolishes clozapine-induced effects between the hM3Dq-mCh and mCh groups (Wilcoxon two-tailed test; $p = 0.805$ for the baseline period, $p = 0.937$ for the transient period, and $p = 0.978$ for the active period).

*$p < 0.05$; ****$p < 0.0001$; NS, not significant. hM3Dq-mCh, n = 11; mCh, n = 7. See also Figure S2.

across the top 10% connections of the brain area of interest (based on FC strength at baseline Figure 3C; see Figures S3A–S3C for a more detailed evaluation of other sparsity levels). This index has been used previously for quantifying connectivity alterations in psychiatric disorders (Yang et al., 2016) or pharmacologically induced changes in connectivity (Preller et al., 2018).

As expected, the NMI varied across brain areas (Figures 3D and 3E; full list in Table S1). The strongest variations occurred in regions that are densely innervated by the LC, such as the primary sensory and somatomotor areas (Bouret and Sara, 2002), the *claustrum* (Crick and Koch, 2005), the prefrontal cortex (; notably the agranular insular cortex, the pre- and infralimbic cortices, the frontal pole, and anterior cingulate areas) (Arnsten, 2009; Hirschberg et al., 2017), several nuclei of the amygdala (McCall et al., 2017), the thalamus (Beas et al., 2018), and the association cortex (Arnsten, 2009; Figures 3D and 3E).

The LC is a bilateral structure, and each locus primarily projects ipsilaterally. Thus, we tested whether our LC stimulation would similarly affect the spatial patterns of FC within the left and the right hemispheres. We found remarkably similar changes in FC (Figures S3D–S3F) on each side. The distribution of the effect size for all edges is right-skewed in both the left and right hemisphere (Figures S3D and S3E), demonstrating increased connectivity after LC activation. Further, the changes in each node expressed with the NMI were highly linearly correlated between the left and right hemisphere (Pearson's correlation = 0.7764, $p < 0.0001$; Figure S3F).

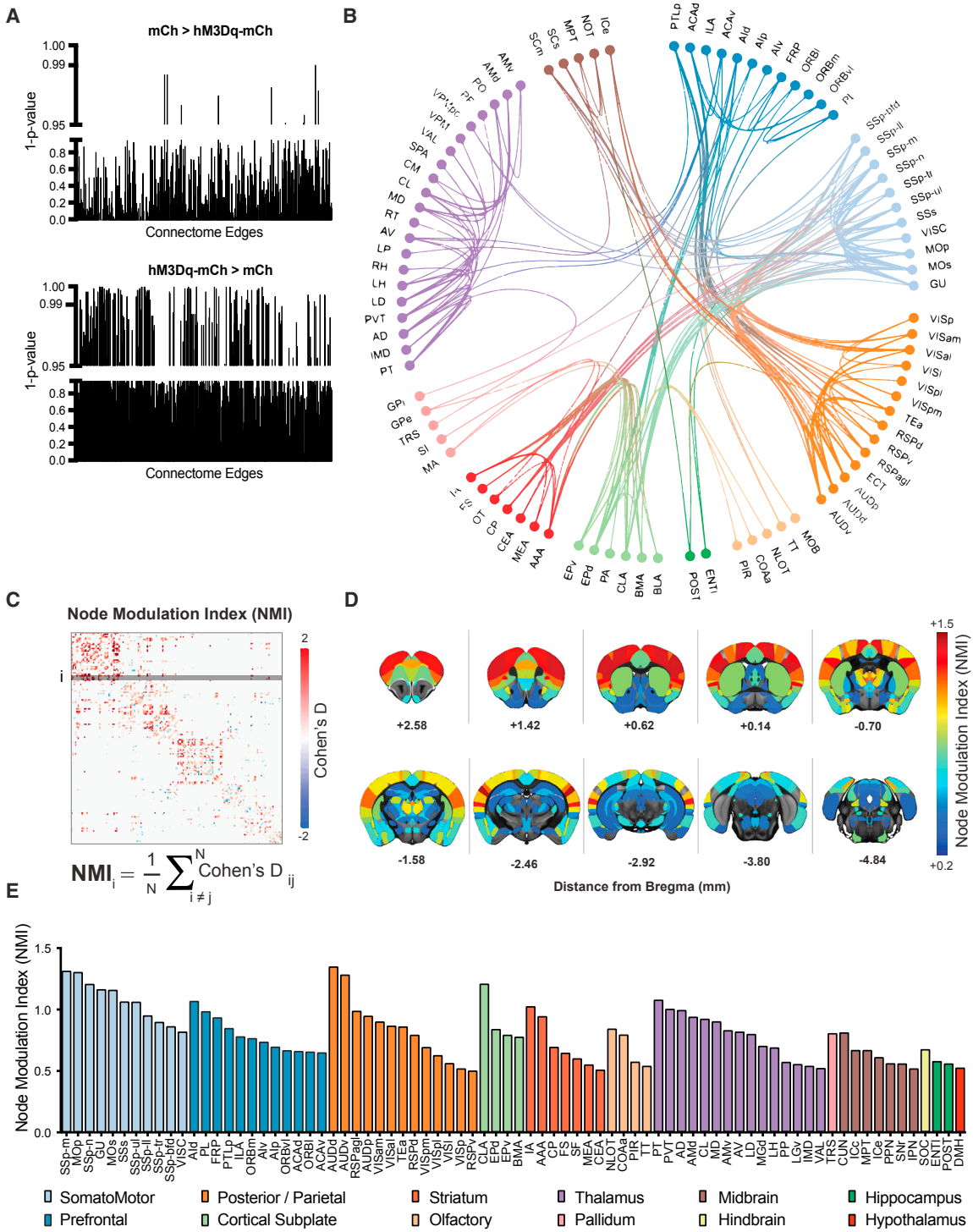

Figure 3. A Whole-Brain Map Showing the Connectome after DREADD-Induced LC Activation

(A) Randomized non-parametric statistics report a drastic shift toward hyperconnectivity in the hM3D(Gq)-mCh group after clozapine injection (15-min bins).

(B) Circos plot showing the anatomical location of hyperconnected edges in response to LC activation ($p < 0.05$, network-based statistics, FWE-corrected).

(C) Node modulation index (NMI), calculated as the averaged effect size in each brain area (165 ROIs based on the Allen common coordinate framework).

(D) Rendering of NMI in Allen MRI space, revealing a heterogeneous distribution across brain regions.

(E) Bar plots representing all ROIs with an NMI of more than 0.5 (moderate to strong effect). See the full ROI list in Table S1.

See also Figure S3 and Table S1.

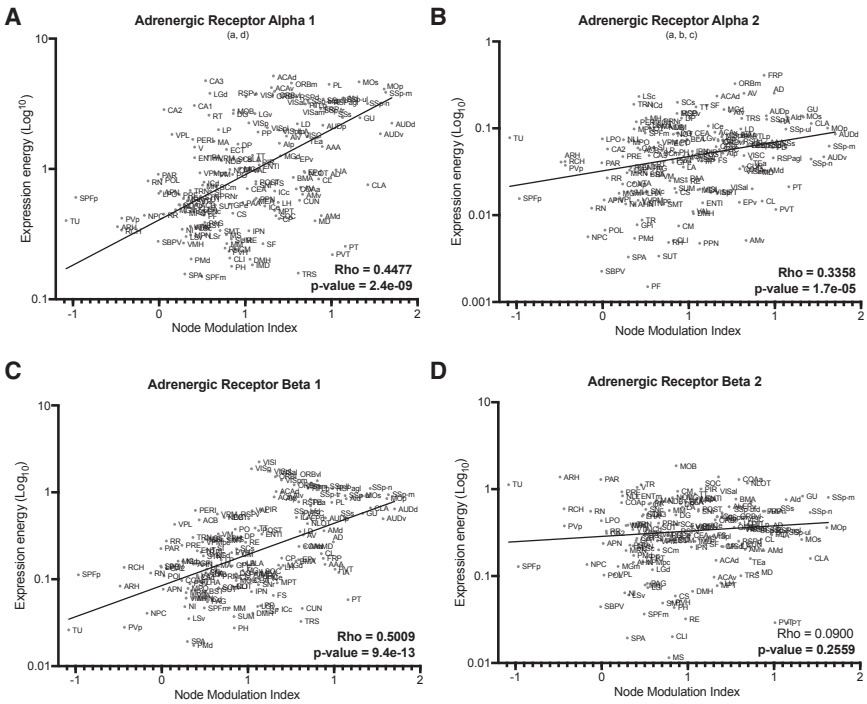

Figure 4. FC Changes after LC-NE Activation Spatially Correlate with Adrenergic Receptor Gene Expression

Spearman correlation coefficients, rho, and associated p value (FDR-corrected) between the node modulation index and the transcriptional maps of genes coding the (A) alpha-1 adrenergic receptor, (B) alpha-2 adrenergic receptor, (C) beta-1 adrenergic receptor, and (D) beta-2 adrenergic receptor. Gene expression data were obtained from the Allen Mouse Brain Atlas and measured using *in situ* hybridization. Transcriptional levels across a macroscopic cortical area were summarized and plotted as the mean in-situ hybridization (ISH) intensity across voxels of that brain area, or "expression energy." See also Figure S4 and Table S2.

We then took advantage of the unique availability of molecular data in the same mouse strain and asked whether the anatomical heterogeneity found in the connectivity-based NMI maps relates to the spatial distribution of adrenergic neurotransmitter receptors in the mouse brain. Gene transcript maps of alpha-1 (subunits a–d), alpha-2 (subunits a–c), beta-1, and beta-2 adrenergic receptors were obtained from the Allen Mouse Brain Atlas (Lein et al., 2007). The similarity to NMI maps was quantified using the Spearman rank correlation coefficient (rho) across all 165 brain areas of the Allen common coordinate framework. After correcting for testing multiple independent hypotheses, we found that the transcriptional maps of all adrenergic receptors display a significant correlation with the NMI, with the exception of beta-2 adrenergic receptors (Figures 4A–4D). All of these correlations display a higher-than-chance Spearman's rho value ($p < 0.0001$ against a null distribution generated using 100,000 random permutations). We additionally compared our NMI maps with all dopamine receptors (D1, D2, D3, D4, and D5), serotonin receptors (*Htr1*, *Htr2*, *Htr3*, *Htr4*, *Htr5*, *Htr6*, and *Htr7*), and cholinergic receptors (muscarinic 1, 2, 3, 4, and 5 and nicotinic alpha-1, alpha-4, alpha-6, alpha-7, beta-1, beta-2, delta, epsilon, and gamma) to assess the specificity of our results (Figure S4). We found a significant Spearman's correlation with both D1 (rho = 0.4014, false-discovery rate corrected p value [p_{FDR}] = $9.11e^{-7}$) and D4 (rho = 0.3789, $p_{FDR} = 3.12e^{-6}$) receptors, which survived permutation testing and false discovery rate (FDR) correction (Figures S4B and S4C), but not with D2, D3, and D5 (Figure S4A). We also found significant correlations with cholinergic nicotinic alpha-1 (rho = 0.3302, $p_{FDR} = 6.38e^{-5}$) and gamma subunits (rho = 0.3887, $p_{FDR} = 1.85e^{-6}$) (Figures S4D and S4E), whereas none of the cholinergic muscarinic receptors or serotonin receptors exhibited correlations above chance level (Figure S4A). To account for spatial co-expression of different receptor types, we performed control analyses where dopaminergic, cholinergic, or adrenergic receptors were added as co-variates into different partial correlation analysis models (see Table S2 for details). We still found strong correlations between NMI and the spatial distribution of adrenergic beta-1 (rho = 0.2623, $p_{FDR} = 7.75e^{-4}$) and alpha-1 (rho = 0.2519, $p = 4.11e^{-3}$) receptors and moderate correlations between NMI and dopamine receptors D1 (rho = 0.2005, p_{FDR} = 0.0179) and D4 (rho = 0.2219, $p_{FDR} = 0.0063$). By contrast, none of the correlations between NMI and the nicotinic cholinergic receptor distributions remained significant when we entered adrenergic receptor distributions as co-variates into the model (Table S2). This analysis suggests that the correlation between nicotinic cholinergic receptors and NMI might have been driven by the spatial co-expression of adrenergic beta-1 and alpha-1 receptors. Overall, these results represent the first brain-wide FC mapping in response to LC activation, revealing an anatomically specific connectomic fingerprint of LC hyperactivity that maps well onto the spatial distribution of specific adrenergic receptors and dopamine receptors.

LC Increased Connectivity within Large-Scale Resting-State Networks

So far, our data-driven analyses focused on changes in connectivity between anatomically defined pairs of brain regions. However, it is well known that there are sets of brain areas, so-called resting-state networks (RSNs) that exhibit synchronous neural activity and can be consistently identified in the mammalian brain. Connectivity strength within a network can be quantified as the relative synchronization of BOLD activity across all voxels forming an RSN, and this measurement has been linked to local electrophysiological properties, behavioral performance, and severity of neurological disease (Rosazza and Minati, 2011). Here we examined whether LC activation influences synchronization within large-scale RSNs by calculating the spatial extent

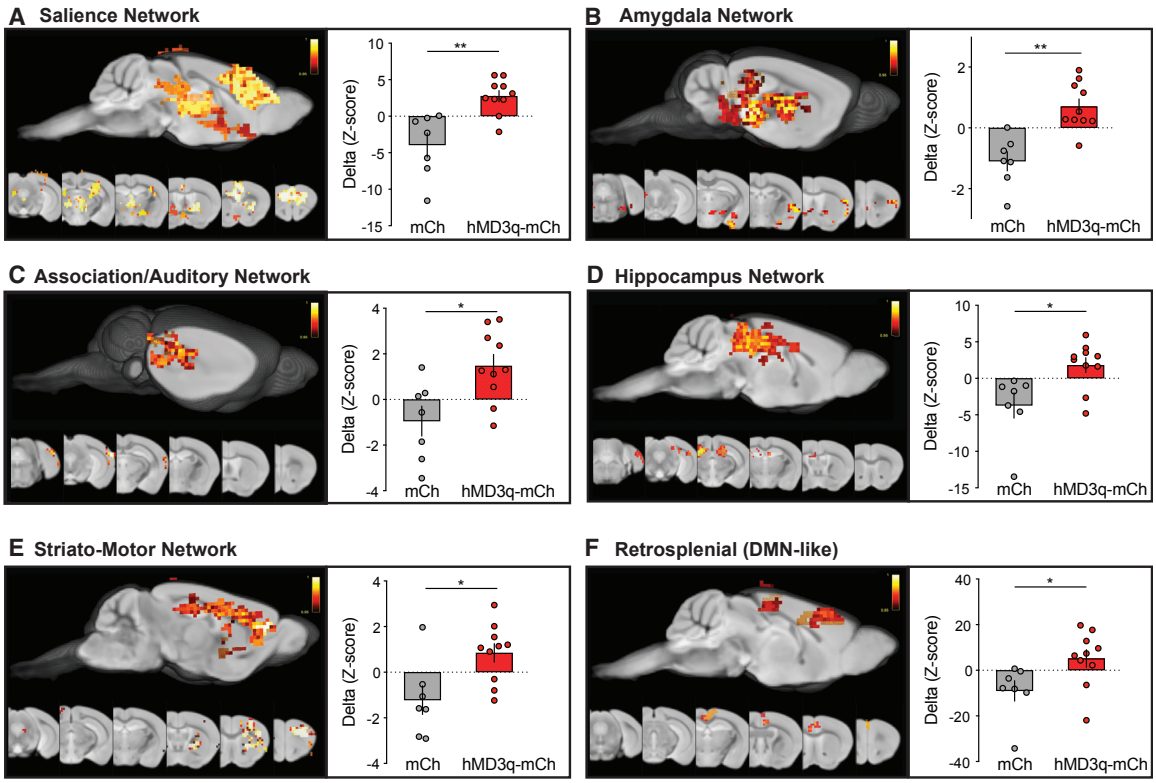

Figure 5. Rapid Changes in Resting-State Network (RSN) Connectivity after LC Activation

Voxel-wise dual regression analysis revealed clusters of significant "group × time interactions" in 6 of 13 RSN ($p < 0.05$, TFCE-corrected). A linear mixed model showed significant network strength increases in the hM3Dq-mCh group compared with mCh control mice after clozapine injection. Bar plots represent mean ± SEM. *$p < 0.05$, **$p < 0.01$ (FDR-corrected).

and connectivity strength for 13 maximally independent RSNs of the mouse brain. The topography of the RSNs was obtained from an independent cohort of wild-type mice (for a complete list and spatial distribution of the networks obtained with independent component analysis, refer to Zerbi et al., 2015). Overall effects within each RSN are determined by measuring a connectivity strength index (using a linear mixed model; Zerbi et al., 2018). Moreover, we investigated which voxels within each RSN significantly changed their level of synchronization upon LC-NE stimulation (using a dual regression approach).

In 6 of 13 RSNs, we found significant group × time interactions resulting from an increase of within-network connectivity in the hM3Dq-mCh group, which was in stark contrast to the slight decrease in connectivity observed in the mCh group (Figure 5). The latter effect is likely attributable to an accumulation of isoflurane over time (Bukhari et al., 2018; Figure S2), which is, however, clearly reversed upon LC activation. We observe the strongest differences in two networks previously linked to LC activity in humans exposed to stress (Hermans et al., 2014): (1) the salience network (hyperconnectivity in the agranular insular area, anterior cingulate, ventro-medial striatum, *accumbens*, *globus pallidus*, parafascicular nucleus of the thalamus, and hippocampus; Figure 5A) and (2) the amygdala network (hyperconnectivity in the basomedial and basolateral amygdala, *claustrum*, sub-thalamic nucleus, and *zona incerta*; Figure 5B). Additionally, LC activation also increased connectivity within the association and auditory network (Figure 5C), the dorsal hippocampus network (Figure 5D), the striato-motor network (Figure 5E), and the antero-posterior retrosplenial network (also known as the default mode network) (Figure 5F). These results suggest that LC activation expands the synchrony of signals in several large-scale networks, most significantly in the salience and amygdala networks. These results are remarkably similar to those in humans, showing that acute stress increases FC within homologous salience and amygdala networks (Hermans et al., 2011; van Marle et al., 2010) in a β-adrenergic receptor-dependent manner (Hermans et al., 2011).

Network Connectivity Changes Correlate with NE and Dopamine Turnover

After completion of the two rs-fMRI sessions, mice were given 1 to 2 weeks to recover (STAR Methods). Eight hM3Dq-mCh mice and five mCh controls were again injected with clozapine (0.03 mg/kg i.p.), and their brains were collected 90 min later to address two important issues. First we wanted to ensure that clozapine exclusively activated noradrenergic LC neurons and that activation occurred in all hM3Dq-mCh mice but not in the mCh controls. Second, we wanted to assess whether LC activation led to measurable NE release in target regions throughout the brain and whether NE levels would correlate

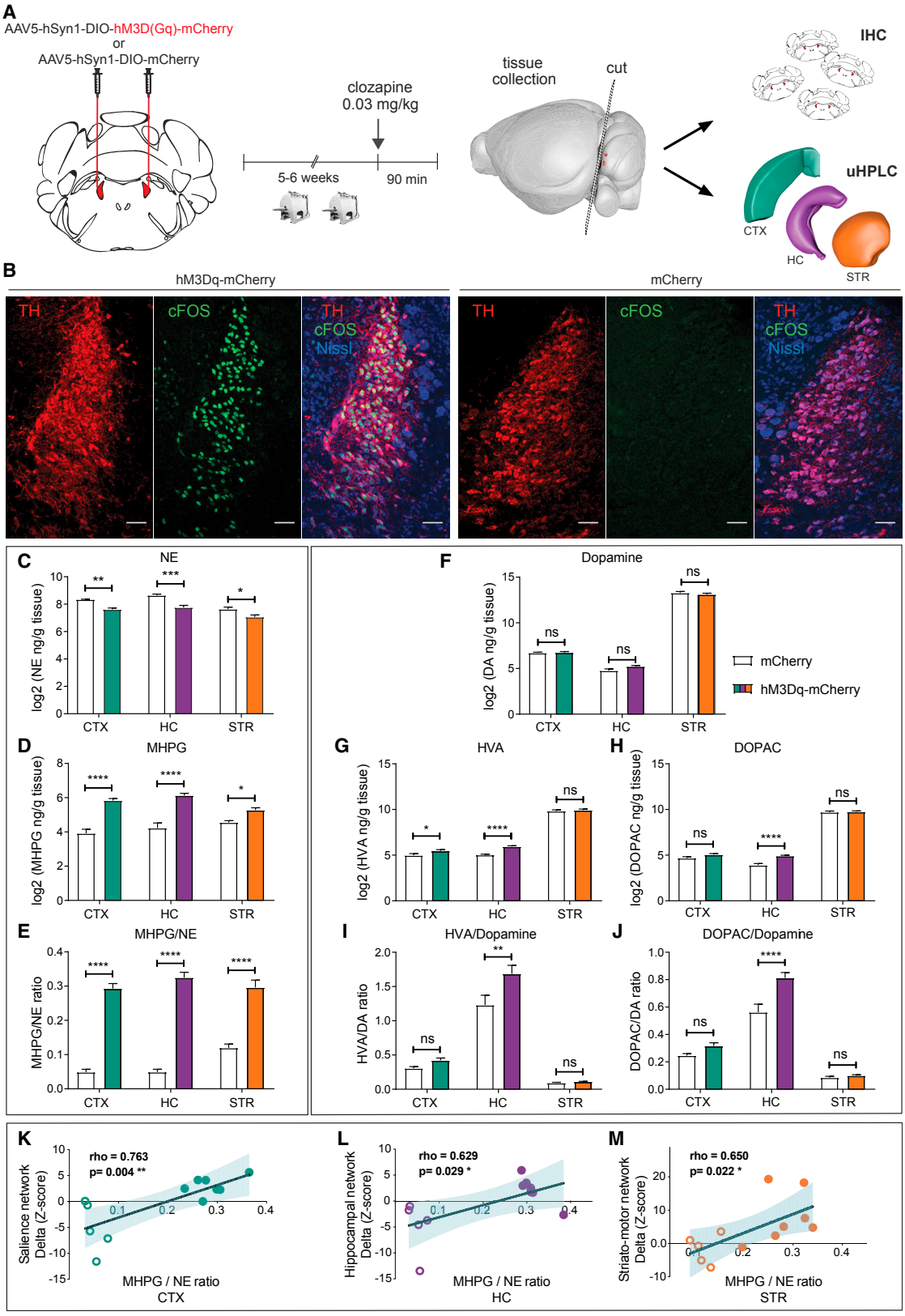

(legend on next page)

with observed changes in network connectivity. To address both these two issues in each individual mouse, we pursued a two-pronged strategy for tissue processing (Figure 6A). Freshly collected brains were split with a razor blade along the superior colliculus to collect one section containing the LC for immunohistochemistry and a second section containing the forebrain. From the forebrain section, we rapidly dissected cerebral cortex, hippocampus, and dorsal striatum on ice. Samples were snap-frozen and processed for analysis of monoamines and their metabolites using reverse-phase ultra-high-performance liquid chromatography (uHPLC) coupled with electrochemical detection (Figure 6A).

Co-labeling for TH and cFOS revealed that clozapine injection only induced a strong and reliable activation of noradrenergic neurons in the LC of hM3Dq-mCh mice (representative image in Figure 6B; sections of all mice in Figure S5). This validates that LC activation was successful in mice undergoing fMRI scans. In parallel, we used uHPLC to measure and quantify the monoaminergic neurotransmitters NE, dopamine (DA), and serotonin (5-HT) as well as their main metabolites 3-methoxy-4-hydroxyphenylglycol (MHPG; a metabolite of NE), homovanillic acid (HVA; a metabolite of DA), 3,4-dihydroxyphenylacetic acid (DOPAC; a metabolite of DA), and 5-hydroxyindoleacetic acid (5-HIAA; a metabolite of 5-HT). Because the measurement in whole tissue does not, per se, differentiate between intra- and extracellular neurotransmitter levels, this approach is mainly targeted toward measuring neurotransmitter ratios of the end-stage metabolite over monoamine (e.g., the MHPG/NE ratio) as an index of neurotransmitter turnover and, thus, neuronal activity. We were able to reliably detect and quantify all measured compounds (see representative chromatographs in Figures S6A and S6B). NE levels decreased in all brain regions (Figure 6C), suggesting that LC activation for 90 min had reduced NE storage vesicles, as would be expected after sustained high-frequency firing. In agreement, MHPG levels increased in all brain regions (Figure 6D), resulting in a very strong increase in catabolic NE turnover (MHPG/NE; Figure 6E). DA levels were not changed in any of the brain regions under investigation (Figure 6F), but we observed a robust increase in both hippocampal HVA and DOPAC (Figures 6G and 6H) and a small but significant increase of HVA in the cortex (Figure 6G). DA turnover ratios (HVA/DA and DOPAC/DA) were increased in the hippocampus but not in the striatum or cortex (Figures 6I and 6J). These results are in line with recent evidence that LC neurons can release DA in certain brain regions, including the hippocampus (Beas et al., 2018; Kempadoo et al., 2016; Smith and Greene, 2012; Takeuchi et al., 2016). Our data newly suggest that DA release from LC neurons may be biased toward the hippocampus compared with the cortex and striatum. Epinephrine, 5-HT, and 5-HT turnover ratios were not altered in any of the brain regions sampled (Figures S6C–S6F).

Because we performed fMRI and uHPLC analyses in the same mice (although with a temporal delay of 1 week and in response to separate injections with clozapine), we were able to conduct a correlation analysis between individual differences in neurotransmitter turnover and corresponding changes in network connectivity. We found positive correlations between the NE and DA turnover ratios in the cortex and changes in FC within the salience network (Figure 6K; Figures S6G and S6J), as well as between NE and DA turnover ratios in the hippocampus and FC in the hippocampus network (Figure 6L; Figures S6H and S6K). NE turnover in the striatum, but not DA turnover, correlated with FC changes in the striato-motor network (Figure 6M; Figures S6I and S6L). Importantly, we observed no correlation between 5-HT levels and turnover and the respective network connectivity changes in any of the brain regions tested (Figures S6M–S6O). These results collectively suggest that the brain network changes we observe with rs-fMRI are tied to the amount of NE and/or DA released in a given region.

LC Neurons Project Sparsely to the Dorsal Striatum (Caudate-Putamen)

Although increased NE turnover in the cortex and hippocampus was expected because of strong innervation by the LC, the increased NE turnover in the dorsal striatum (consisting of the caudate and putamen) (Zeiss, 2005) was surprising because this region is widely thought to be devoid of NE projections (Aston-Jones, 2004; Berridge and Waterhouse, 2003). In agreement with increased striatal NE turnover, we also observed a strong increase in the NMI in the caudate-putamen (Figure 3E) and increased FC within the large-scale striato-motor network (Figure 5E). Thus, we decided to first test whether we could detect noradrenergic axons within the caudate-putamen. We stained for the NET Slc6a2, which is expressed exclusively in noradrenergic cells (Mulvey et al., 2018; Schroeter et al., 2000). Although the caudate-putamen appears to be devoid of norepinephrine transporter (NET) compared with the intense NET staining seen in the adjacent cortex (Figure 7A), we clearly

Figure 6. NE and DA Turnover Induced by LC Activation Correlates with rs-fMRI Data

(A) Outline of the tissue collection strategy following completion of fMRI scans. CTX, cortex; HC, hippocampus; STR, striatum = caudate-putamen.

(B) Representative images of cFOS expression in the LC after clozapine injection in hM3Dq-mCh or mCh mice. Scale bars, 50 μm.

(C–J) Levels of monoaminergic neurotransmitters and their metabolites in the cortex, hippocampus, and striatum. NE was reduced in all brain regions of hM3Dq-mCh mice relative to mCh controls (C; main effect of group: $F(1,33) = 42.48$, $p < 0.0001$), MHPG was increased (D; main effect of group: $F(1,33) = 121.80$, $p < 0.0001$), and the NE turnover ratio (MHPG/NE) was increased (E; main effect of group: $F(1,33) = 291.50$, $p < 0.0001$; two-way ANOVA with Sidak *post hoc* tests). Although there was no difference in the levels of DA (F; main effect for group: $F(1,33) = 0.81$, $p = 0.3748$), its metabolite HVA was increased in the cortex and the hippocampus in hM3Dq-mCh mice (G; significant main effect for group: $F(1,11) = 11.60$, $p = 0.0059$), and DOPAC was increased only in the hippocampus (H; significant main effect for group $F(1,33) = 22.13$, $p < 0.0001$). The DA turnover ratios were only increased in the hippocampus for both HVA/DA (I; main effect of group: $F(1,33) = 8.91$, $p = 0.0053$) and DOPAC/DA (J; main effect of group: $F(1,33) = 19.81$, $p < 0.0001$; two-way ANOVA with Sidak *post hoc* tests).

(K–M) Correlation between FC changes and neurotransmitter levels in the cortex (K), hippocampus (L), and striatum (M). Circles correspond to mCh mice and filled circles to hM3Dq-mCh mice.

*$p < 0.05$, **$p < 0.01$, ***$p < 0.001$, ****$p < 0.0001$. Data represent mean ± SEM. See also Figures S5 and S6.

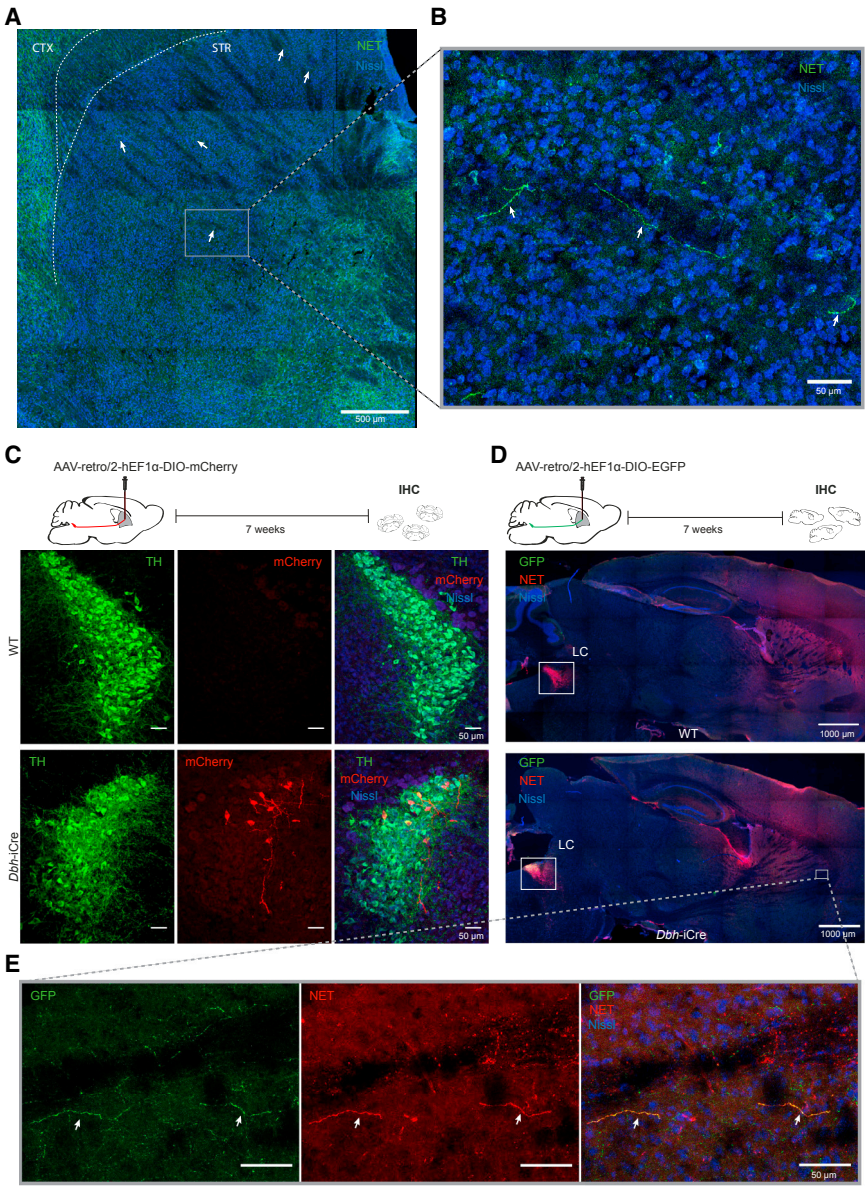

Figure 7. The Dorsal Striatum (Caudate-Putamen) Is Innervated by the LC

(A) Immunohistochemical localization of the norepinephrine transporter (NET) reveals noradrenergic axons in the caudate-putamen (arrows).

(B) Magnification of the box in (A), showing NET+ axons (arrows).

(C) A retro-AAV2 that expresses Cre-dependent mCh was delivered to the dorsolateral caudate-putamen and resulted in mCh+ neurons in the LC of DBH-iCre mice (n = 3) but not in a wild-type mouse (n = 1). Representative pictures from one animal are shown, additional images for all mice are shown in Figure S7.

(D) Stereotactic delivery of a Cre-dependent retro-AAV2 virus expressing EGFP in the dorsolateral caudate-putamen resulted in EGFP+ LC neurons in a DBH-iCre mouse but not in a wild-type mouse.

(E) Magnification of the box in (D), showing the axonal co-localization of NET and EGFP in the caudate-putamen of a DBH-iCre animal. CTX, cortex; STR, striatum.

See also Figure S7.

detected long, thin axons in the caudate-putamen (Figure 7B). To investigate whether these axons originate from LC neurons, we delivered a retrograde AAV2 virus (Tervo et al., 2016) carrying floxed mCh into the dorsolateral caudate-putamen of DBH-iCre mice. Seven weeks after virus injection, we stained the LC and detected a clearly recognizable subset of LC neurons that expressed mCh in transgenic animals (n = 3) but not in a wild-type control animal (n = 1) (representative images from each animal are shown in Figure 7C and Figure S7). We were able to reproduce these findings with a second Cre-dependent retrograde AAV2 virus that expresses EGFP (Figure 7D), which also allowed us to detect axons in the caudate-putamen that were co-labeled with both EGFP and NET (Figure 7E). Together, these data show that there are sparse projections from the LC to the caudate-putamen. These projections could account for the increase in NE levels detected in the striatum after LC stimulation as well as for the increased FC observed in the caudate-putamen and in the large-scale striatomotor network.

DISCUSSION

Revealing the Connectomic Fingerprint of NE Release after LC Activation

Neuromodulatory systems of the brain track and integrate environmental signals, exert powerful control over neuronal function, and are the primary targets of most psychiatric treatment strategies (Avery and Krichmar, 2017; Berton and Nestler, 2006; Lee and Dan, 2012). Human neuroimaging data suggest that noradrenergic neuromodulation dynamically influences long-range neural communication, strengthening specific functional networks to facilitate task performance (Shine et al., 2016, 2019). It is, however, challenging to study the effect of an individual neuromodulatory system across large-scale neuronal networks. Optogenetic and chemogenetic tools, combined with advances in rodent imaging capabilities, now enable us to link circuit-level manipulations to global network changes. Recent studies have used these approaches to show that manipulation of DA (Lohani et al., 2017; Roelofs et al., 2017) and serotonin (Giorgi et al., 2017) release can lead to global activity changes measured by fMRI. We extend these studies by assessing the role of the LC-NE system in assembling and rearranging connectivity within and between well-defined large-scale neuronal systems using rs-fMRI. Our

chemo-connectomic approach establishes the framework necessary to link the activity of neuromodulatory systems to clinically relevant brain signals and their neuroanatomical substrates.

Adrenergic Receptor Distribution as an Organizing Principle Affording "Global Specificity"

Neurons in the LC are topographically organized based on their efferent projections (Aston-Jones, 2004; Schwarz and Luo, 2015), and circuit-based approaches reveal functional specificity of sub-populations of LC neurons (Hirschberg et al., 2017; Uematsu et al., 2017). LC neurons appear to form neuronal ensembles that can be activated in response to isolated sensory stimuli (Totah et al., 2018, 2019). With increasing stimulus strength, more LC ensembles can be activated, leading to global LC activation in response to strong stimuli (such as stress exposure) (Totah et al., 2019). Widespread NE release in response to this global LC activation is commonly thought to act as a broadcast signal that modulates local electrophysiological properties, gearing specific networks toward integrating environmental information, allowing selection or triggering of adequate behaviors (Schwarz and Luo, 2015; Usher et al., 1999). We hypothesized that the distribution of adrenergic receptors enables network-specific effects of global NE release. Indeed, we observed strong correlations between FC and expression levels of alpha-1 and beta-1 adrenergic receptors, which were maintained over and above the effect explained by the distribution of other receptor types. We found weaker correlations with inhibitory adrenergic alpha-2 receptors, dopaminergic D1 and D4 receptors, and cholinergic nicotinic alpha-1 and gamma receptor subunits. Multiple regression analyses indicate that correlations between FC and cholinergic nicotinic receptors and alpha-2 adrenergic receptors may be driven by spatial co-expression with alpha-1 and beta-1 adrenergic receptors. NE has a much higher affinity for alpha-2 adrenergic receptors; thus, their signaling contribution is smaller during strong NE release, which activates alpha-1 and beta-1 receptors (Arnsten, 2009). However, definitive conclusions regarding the contribution of individual receptors to the observed effects on connectivity would require local administration of specific receptor antagonists. The absence of a correlation with beta-2 adrenergic receptors was unexpected, given that both beta-1 and beta-2 adrenergic receptors are ubiquitously expressed and have similar binding affinity for NE (Ramos and Arnsten, 2007). It is possible that beta-2 adrenergic receptors indeed do not play a role in the NE-induced effects on network connectivity because contrasting effects of beta-1 and beta-2 adrenergic receptors on working memory performance have been reported previously (Ramos et al., 2005, 2008). However, it is also possible that technical limitations mask an involvement of beta-2 adrenergic receptors, given that we attempt to align our connectivity data with publicly available spatial gene expression maps of individual receptor densities. Compared with previous work that has correlated connectivity measures of a brain area with the transcriptional profile across a large number of genes (Fulcher and Fornito, 2016; Rubinov et al., 2015), correlations with a single gene are more susceptible to noise in gene expression data. Therefore, we believe that the strong correlations between NMI and beta-1 and alpha-1 adrenergic receptors are evidence for a robust relationship, whereas weak gene-NMI correlations should be interpreted with caution and cannot be used to infer the absence of an association.

LC Activation Recapitulates Many of the Complex Effects Triggered by Stress Exposure

Modern theories of LC function propose that LC activation serves to optimize the trade-off between exploitation and exploration, with strong, global LC activity causing interruption of ongoing activity to enable the selection of appropriate behaviors (Aston-Jones and Cohen, 2005). Global LC activity is triggered by noxious and/or stressful stimuli (Berridge and Waterhouse, 2003; Valentino and Van Bockstaele, 2008), which induce anxiety and reduce exploratory activity, through circuits involving the amygdala and prefrontal cortex (Hirschberg et al., 2017; Li et al., 2018; McCall et al., 2015, 2017; Uematsu et al., 2017). Our DREADD-induced activation of the LC similarly reduces exploratory activity, increases anxiety, and globally induces cFOS expression throughout the LC. Therefore, our global LC activation likely resembles peak LC activity that would normally be triggered by stressful stimuli.

Our data are well in line with findings in humans where acute stress exposures (induced by aversive movies or social stressors) increased FC in the salience network (van Marle et al., 2010) and default mode network (Vaisvaser et al., 2013). Similarly, acute stress leads to increased interconnectivity and positive BOLD responses within several cortical regions related to salience processing (frontoinsular, anterior cingulate, inferotemporal, and temporoparietal regions) and subcortical regions (amygdala, striatum, thalamus, hypothalamus, hippocampus, and midbrain) as a function of stress response magnitude (Hermans et al., 2011; van Oort et al., 2017; Seo et al., 2011; Sinha et al., 2004). Notably, increased connectivity in the salience network was blocked by systemic administration of a β-adrenergic receptor antagonist (propranolol) (Hermans et al., 2011). Given that LC activation is only one aspect of the highly complex changes observed during an acute stress response (Joëls and Baram, 2009), and considering that our analyses were performed in lightly anesthetized mice, it is remarkable that our results for the salience network, the amygdala network, and also the default mode network closely resemble fMRI and rs-fMRI findings described after acute stress exposures in humans (Hermans et al., 2014; van Oort et al., 2017; Figure 5). Because we selectively manipulated LC activity with DREADDs, our results causally show that LC activation rapidly reorganizes FC within specific large-scale networks. The rapid onset of the connectomic effects within minutes after LC activation points toward a direct, causal effect mediated by NE release throughout the forebrain.

Long-lasting hyperactivity of the LC is often observed after severe or chronic stress exposure (Borodovitsyna et al., 2018; Mana and Grace, 1997) and is considered a hallmark feature of post-traumatic stress disorder (PTSD) (Naegeli et al., 2018; Pietrzak et al., 2013). Two recent rs-fMRI studies showed, in both rats and mice, that chronic stress exposure results in large-range increases in functional network connectivity for regions including the prelimbic and infralimbic areas, the amygdala, the cingulate

cortex, and the hippocampus (Grandjean et al., 2016; Magalhães et al., 2018). In PTSD patients, fMRI reveals network-wide changes in the amygdala, *insula*, hippocampus, and anterior cingulate cortex (Fitzgerald et al., 2018; Liberzon and Phan, 2003). Therefore, the changes observed after chronic stress exposure in rodents and in PTSD patients are strikingly similar to the effects of selective LC stimulation. Hyperactivity of the LC is only one aspect of stress-related pathologies, but our data provide additional evidence that modulating LC activity might be a promising therapeutic approach (Bangasser and Valentino, 2014; Borodovitsyna et al., 2018).

One limitation of our approach is that fMRI requires anesthesia; thus, we cannot assess how selective LC manipulations would modulate network activity and/or connectivity during task performance. NE modulates ongoing neural activity and controls neuronal gain (signal-to-noise ratio) (Mather et al., 2016; Sara and Bouret, 2012). Further, the effects of NE on brain function are task dependent, and recent work on memory consolidation shows that noradrenergic activity in the amygdala itself influences large-scale networks (Barsegyan et al., 2019). Therefore, the role of NE on brain region-specific activity during task performance needs to be carefully assessed in future studies, when task-relevant networks are specifically engaged while others are suppressed.

FC after LC Activation Involves DA Release and DA Receptors

Several recent reports have shown that DA can be co-released from LC terminals in the hippocampus (Kempadoo et al., 2016; Smith and Greene, 2012; Takeuchi et al., 2016) and thalamus (Beas et al., 2018). We also detected a strong increase in DA turnover in the hippocampus and a subtle increase in the cortex. Because our cortex samples contained heterogeneous regions, it is likely that specific cortical subregions (e.g., the mPFC) display stronger changes in DA turnover. In concordance with our data, previous microdialysis experiments have detected release of both DA and NE in the mPFC after chemical or electrical activation of the LC, whereas the same stimulations increased NE but not DA in the *nucleus accumbens* and caudate nucleus (Devoto et al., 2005b, 2005a; Kawahara et al., 2001). Together, our data provide new evidence for a regionally restricted role of DA release in response to LC stimulation. Future studies will have to test whether all LC neurons (or only selected sub-populations with specific projection targets) are able to release DA and whether specific interactions at the projection site are required to enable DA release. Finally, it remains unclear whether this co-release occurs under physiological conditions because evidence suggests that it depends on the firing rate of individual LC neurons (Devoto et al., 2005b).

LC-Induced Synchronization in the Dorsal Striatum (Caudate-Putamen)

Although close interactions between dopaminergic and noradrenergic systems have long been recognized (Antelman and Caggiula, 1977), the dorsal striatum (caudate-putamen) is widely thought to be devoid of noradrenergic projections (Aston-Jones, 2004; Berridge and Waterhouse, 2003), and, indeed, staining for NET (Figure 7A) or DBH (Swanson and Hartman, 1975) shows strong depletion in the caudate-putamen. Given these data, we were surprised when our connectome analysis revealed that LC activation increased the strength of caudate-putamen connectivity (Figure 3C). Further, we observed synchronization of rs-fMRI activity in the striato-motor network, which positively correlated with increased NE turnover in the same region (Figure 6M). Indeed, several studies have shown fairly high levels of NE (Schallert et al., 1978) in the caudate-putamen as well as an extracellular striatal NE increase after mild stress (handling) (Ihalainen et al., 1999) or LC stimulation (Devoto et al., 2005a). Alpha-1, alpha-2, and beta-1 adrenergic receptors are abundantly expressed on striatal pre- and post-synaptic cells (Hara et al., 2010; Nicholas et al., 1996; Paschalis et al., 2009; Pisani et al., 2003; Rommelfanger et al., 2009), and beta-adrenergic receptor binding density is very high in the caudate-putamen of rodents and humans (Bylund and Snyder, 1976; Palacios and Kuhar, 1980; Reisine et al., 1979). Our results show that a considerable number of LC neurons directly project to the caudate-putamen, which is in line with early retrograde tracing work (Mason and Fibiger, 1979) but is rarely recognized in more recent literature. These findings may be relevant for Parkinson's disease, where involvement of the LC-NE system is increasingly being recognized (Vermeiren and De Deyn, 2017; Weinshenker, 2018).

Conclusions

Using the novel chemo-connectomics approach presented here, we provide the first brain-wide analysis of connectome reconfiguration in response to selective LC activation. We show profound, rapid, and specific activation of large-scale networks related to salience processing that occurs within minutes after clozapine administration, specifically in mice expressing DREADDs. These effects are observed similarly in each hemisphere, and they are blocked by activating presynaptic, autoinhibitory alpha-2 adrenergic receptors. Shifts in large-scale network connectivity correlate spatially with the distribution of adrenergic and dopaminergic receptor levels and with (post-mortem) measurements of NE, DA, and their metabolites in a within-subject design. These network effects are accompanied by increased pupil size and heightened anxiety, suggesting that the observed changes in brain network organization ultimately serve to promote vigilance and threat detection.

STAR★METHODS

Detailed methods are provided in the online version of this paper and include the following:

- KEY RESOURCES TABLE
- LEAD CONTACT AND MATERIALS AVAILABILITY
- EXPERIMENTAL MODEL AND SUBJECT DETAILS
- METHOD DETAILS
  - Stereotaxic brain injections
  - Pupil recordings
  - Behavioral testing
  - Tissue collection and processing
  - MRI
  - Ultra-high performance liquid chromatography (uHPLC)

SUPPLEMENTAL INFORMATION

Supplemental Information can be found online at https://doi.org/10.1016/j.neuron.2019.05.034.

ACKNOWLEDGMENTS

We thank Han-Yu Lin for genotyping and help with image analysis and all animal caretakers of the EPIC animal facility. We thank Jean-Charles Paterna from the Viral Vector Facility (VVF) of the Neuroscience Center Zürich, a joint competence center of ETH Zürich and the University of Zürich, for producing viral vectors and viral vector plasmids. We thank Prof. Isabelle Mansuy for providing support and space, Dr. Ben Fulcher for providing gene expression data and help with the correlational analyses, and Pierre-Luc Germain for feedback on statistical analyses. We thank Tilo A. Gschwind for guidance on cFOS staining, Ladina Hösli for advice during the rotarod experiments, and Prof. Markus Rudin for use of the MRI facilities. V.Z. is supported by ETH career seed grant SEED-42 54 16-1 and by SNSF AMBIZIONE PZ00P3_173984/1. A.F.-S. is supported by Neuroscience Center Zürich PhD grant, the Swiss Foundation for Excellence and Talent in Biomedical Research, and the EMDO Foundation. M.M. is supported by research grant ETH-38 16-2. The lab of J.B. is funded by ETH Zürich, SNSF project grant 310030_172889/1, the Forschungskredit of the University of Zürich grant FK-15-035, the Vontobel Foundation, the Novartis Foundation for Medical-Biological Research, the Olga Mayenfisch Foundation, and the Betty and David Koetser Foundation for Brain Research. Funding of uHPLC analyses was covered by Alzheimer Foundation Belgium (SAO-FRA) research grant P#16003 and support of Joint Programming Initiative Neurodegenerative Diseases (JPND) multinational research project HEROES – ZonMw project 733051072.

AUTHOR CONTRIBUTIONS

Conceptualization, V.Z., A.F.-S., N.W., and J.B.; Methodology, V.Z., A.F.-S., K.D.F., M.M., O.S., and L.v.Z.; Investigation, V.Z., A.F.-S., M.M., Y.V., M.P., and O.S.; Writing – Original Draft, V.Z., A.F.-S., Y.V., N.W., and J.B.; Writing – Review & Editing, V.Z., A.F.-S., M.M., Y.V., O.S., M.P., K.D.F., L.v.Z., B.W., P.P.D.D., N.W., and J.B.; Funding Acquisition, V.Z., A.F.-S., B.W., P.P.D.D., N.W., and J.B.; Resources, B.W. and P.P.D.D.; Supervision, V.Z., N.W., and J.B.

DECLARATION OF INTERESTS

The authors declare no competing interests.

Received: February 8, 2019
Revised: April 15, 2019
Accepted: May 21, 2019
Published: June 18, 2019

REFERENCES

Aksenov, D.P., Li, L., Miller, M.J., Iordanescu, G., and Wyrwicz, A.M. (2015). Effects of anesthesia on BOLD signal and neuronal activity in the somatosensory cortex. J. Cereb. Blood Flow Metab. *35*, 1819–1826.

Antelman, S.M., and Caggiula, A.R. (1977). Norepinephrine-dopamine interactions and behavior. Science *195*, 646–653.

Armbruster, B.N., Li, X., Pausch, M.H., Herlitze, S., and Roth, B.L. (2007). Evolving the lock to fit the key to create a family of G protein-coupled receptors potently activated by an inert ligand. Proc. Natl. Acad. Sci. USA *104*, 5163–5168.

Arnsten, A.F.T. (2009). Stress signalling pathways that impair prefrontal cortex structure and function. Nat. Rev. Neurosci. *10*, 410–422.

Aston-Jones, G. (2004). Locus coeruleus, A5 and A7 noradrenergic cell groups. In The Rat Nervous System, Third Edition, G. Paxinos, ed. (Academic Press), pp. 259–294.

Aston-Jones, G., and Cohen, J.D. (2005). An integrative theory of locus coeruleus-norepinephrine function: adaptive gain and optimal performance. Annu. Rev. Neurosci. *28*, 403–450.

Avery, M.C., and Krichmar, J.L. (2017). Neuromodulatory Systems and Their Interactions: A Review of Models, Theories, and Experiments. Front. Neural Circuits *11*, 108.

Bakker, R., Tiesinga, P., and Kötter, R. (2015). The Scalable Brain Atlas: Instant Web-Based Access to Public Brain Atlases and Related Content. Neuroinformatics *13*, 353–366.

Bangasser, D.A., and Valentino, R.J. (2014). Sex differences in stress-related psychiatric disorders: neurobiological perspectives. Front. Neuroendocrinol. *35*, 303–319.

Bangasser, D.A., Eck, S.R., and Ordoñes Sanchez, E. (2019). Sex differences in stress reactivity in arousal and attention systems. Neuropsychopharmacology *44*, 129–139.

Barsegyan, A., Mirone, G., Ronzoni, G., Guo, C., Song, Q., van Kuppeveld, D., Schut, E.H.S., Atsak, P., Teurlings, S., McGaugh, J.L., et al. (2019). Glucocorticoid enhancement of recognition memory via basolateral amygdala-driven facilitation of prelimbic cortex interactions. Proc. Natl. Acad. Sci. USA *116*, 7077–7082.

Beas, B.S., Wright, B.J., Skirzewski, M., Leng, Y., Hyun, J.H., Koita, O., Ringelberg, N., Kwon, H.B., Buonanno, A., and Penzo, M.A. (2018). The locus coeruleus drives disinhibition in the midline thalamus via a dopaminergic mechanism. Nat. Neurosci. *21*, 963–973.

Berridge, C.W., and Waterhouse, B.D. (2003). The locus coeruleus-noradrenergic system: modulation of behavioral state and state-dependent cognitive processes. Brain Res. Brain Res. Rev. *42*, 33–84.

Berton, O., and Nestler, E.J. (2006). New approaches to antidepressant drug discovery: beyond monoamines. Nat. Rev. Neurosci. *7*, 137–151.

Borodovitsyna, O., Joshi, N., and Chandler, D. (2018). Persistent Stress-Induced Neuroplastic Changes in the Locus Coeruleus/Norepinephrine System. Neural Plast. *2018*, 1892570.

Bouret, S., and Sara, S.J. (2002). Locus coeruleus activation modulates firing rate and temporal organization of odour-induced single-cell responses in rat piriform cortex. Eur. J. Neurosci. *16*, 2371–2382.

Bukhari, Q., Schroeter, A., and Rudin, M. (2018). Increasing isoflurane dose reduces homotopic correlation and functional segregation of brain networks in mice as revealed by resting-state fMRI. Sci. Rep. *8*, 10591.

Bullmore, E., and Sporns, O. (2009). Complex brain networks: graph theoretical analysis of structural and functional systems. Nat. Rev. Neurosci. *10*, 186–198.

Bylund, D.B., and Snyder, S.H. (1976). Beta adrenergic receptor binding in membrane preparations from mammalian brain. Mol. Pharmacol. *12*, 568–580.

Carter, M.E., Yizhar, O., Chikahisa, S., Nguyen, H., Adamantidis, A., Nishino, S., Deisseroth, K., and de Lecea, L. (2010). Tuning arousal with optogenetic modulation of locus coeruleus neurons. Nat. Neurosci. *13*, 1526–1533.

Corbetta, M., Patel, G., and Shulman, G.L. (2008). The reorienting system of the human brain: from environment to theory of mind. Neuron *58*, 306–324.

Crick, F.C., and Koch, C. (2005). What is the function of the claustrum? Philos. Trans. R. Soc. B Biol. Sci. *360*, 1271–1279.

Devoto, P., Flore, G., Saba, P., Fà, M., and Gessa, G.L. (2005a). Stimulation of the locus coeruleus elicits noradrenaline and dopamine release in the medial prefrontal and parietal cortex. J. Neurochem. *92*, 368–374.

Devoto, P., Flore, G., Saba, P., Fà, M., and Gessa, G.L. (2005b). Co-release of noradrenaline and dopamine in the cerebral cortex elicited by single train and repeated train stimulation of the locus coeruleus. BMC Neurosci. *6*, 31.

Fitzgerald, J.M., DiGangi, J.A., and Phan, K.L. (2018). Functional Neuroanatomy of Emotion and Its Regulation in PTSD. Harv. Rev. Psychiatry *26*, 116–128.

Fortress, A.M., Hamlett, E.D., Vazey, E.M., Aston-Jones, G., Cass, W.A., Boger, H.A., and Granholm, A.C.E. (2015). Designer receptors enhance memory in a mouse model of Down syndrome. J. Neurosci. *35*, 1343–1353.

Fulcher, B.D., and Fornito, A. (2016). A transcriptional signature of hub connectivity in the mouse connectome. Proc. Natl. Acad. Sci. USA *113*, 1435–1440.

Fulcher, B.D., Murray, J.D., Zerbi, V., and Wang, X.J. (2019). Multimodal gradients across mouse cortex. Proc. Natl. Acad. Sci. U.S.A. *116*, 4689–4695.

Giorgi, A., Migliarini, S., Galbusera, A., Maddaloni, G., Mereu, M., Margiani, G., Gritti, M., Landi, S., Trovato, F., Bertozzi, S.M., et al. (2017). Brain-wide Mapping of Endogenous Serotonergic Transmission via Chemogenetic fMRI. Cell Rep. *21*, 910–918.

Gomez, J.L., Bonaventura, J., Lesniak, W., Mathews, W.B., Sysa-Shah, P., Rodriguez, L.A., Ellis, R.J., Richie, C.T., Harvey, B.K., Dannals, R.F., et al. (2017). Chemogenetics revealed: DREADD occupancy and activation via converted clozapine. Science *503*, 503–507.

Grandjean, J., Schroeter, A., Batata, I., and Rudin, M. (2014). Optimization of anesthesia protocol for resting-state fMRI in mice based on differential effects of anesthetics on functional connectivity patterns. Neuroimage *102*, 838–847.

Grandjean, J., Azzinnari, D., Seuwen, A., Sigrist, H., Seifritz, E., Pryce, C.R., and Rudin, M. (2016). Chronic psychosocial stress in mice leads to changes in brain functional connectivity and metabolite levels comparable to human depression. Neuroimage *142*, 544–552.

Hara, M., Fukui, R., Hieda, E., Kuroiwa, M., Bateup, H.S., Kano, T., Greengard, P., and Nishi, A. (2010). Role of adrenoceptors in the regulation of dopamine/DARPP-32 signaling in neostriatal neurons. J. Neurochem. *113*, 1046–1059.

Hermans, E.J., van Marle, H.J.F., Ossewaarde, L., Henckens, M.J.A.G., Qin, S., van Kesteren, M.T.R., Schoots, V.C., Cousijn, H., Rijpkema, M., Oostenveld, R., and Fernández, G. (2011). Stress-related noradrenergic activity prompts large-scale neural network reconfiguration. Science *334*, 1151–1153.

Hermans, E.J., Henckens, M.J.A.G., Joëls, M., and Fernández, G. (2014). Dynamic adaptation of large-scale brain networks in response to acute stressors. Trends Neurosci. *37*, 304–314.

Hirschberg, S., Li, Y., Randall, A., Kremer, E.J., Pickering, A.E., Kingdom, U., and Kingdom, U. (2017). Functional dichotomy in spinal- vs prefrontal-projecting locus coeruleus modules splits descending noradrenergic analgesia from ascending aversion and anxiety in rats. Elife *6*, e29808.

Ihalainen, J.A., Riekkinen, P., Jr., and Feenstra, M.G.P. (1999). Comparison of dopamine and noradrenaline release in mouse prefrontal cortex, striatum and hippocampus using microdialysis. Neurosci. Lett. *277*, 71–74.

Isingrini, E., Perret, L., Rainer, Q., Amilhon, B., Guma, E., Tanti, A., Martin, G., Robinson, J., Moquin, L., Marti, F., et al. (2016). Resilience to chronic stress is mediated by noradrenergic regulation of dopamine neurons. Nat. Neurosci. *19*, 560–563.

Joëls, M., and Baram, T.Z. (2009). The neuro-symphony of stress. Nat. Rev. Neurosci. *10*, 459–466.

Jorm, C.M., and Stamford, J.A. (1993). Actions of the hypnotic anaesthetic, dexmedetomidine, on noradrenaline release and cell firing in rat locus coeruleus slices. Br. J. Anaesth. *71*, 447–449.

Kawahara, H., Kawahara, Y., and Westerink, B.H.C. (2001). The noradrenaline-dopamine interaction in the rat medial prefrontal cortex studied by multi-probe microdialysis. Eur. J. Pharmacol. *418*, 177–186.

Kempadoo, K.A., Mosharov, E.V., Choi, S.J., Sulzer, D., and Kandel, E.R. (2016). Dopamine release from the locus coeruleus to the dorsal hippocampus promotes spatial learning and memory. Proc. Natl. Acad. Sci. USA *113*, 14835–14840.

Lakhlani, P.P., MacMillan, L.B., Guo, T.Z., McCool, B.A., Lovinger, D.M., Maze, M., and Limbird, L.E. (1997). Substitution of a mutant α2a-adrenergic receptor via "hit and run" gene targeting reveals the role of this subtype in sedative, analgesic, and anesthetic-sparing responses in vivo. Proc. Natl. Acad. Sci. USA *94*, 9950–9955.

Lee, S.H., and Dan, Y. (2012). Neuromodulation of brain states. Neuron *76*, 209–222.

Lein, E.S., Hawrylycz, M.J., Ao, N., Ayres, M., Bensinger, A., Bernard, A., Boe, A.F., Boguski, M.S., Brockway, K.S., Byrnes, E.J., et al. (2007). Genome-wide atlas of gene expression in the adult mouse brain. Nature *445*, 168–176.

Li, L., Feng, X., Zhou, Z., Zhang, H., Shi, Q., Lei, Z., Shen, P., Yang, Q., Zhao, B., Chen, S., et al. (2018). Stress Accelerates Defensive Responses to Looming in Mice and Involves a Locus Coeruleus-Superior Colliculus Projection. Curr. Biol. *28*, 859–871.e5.

Liberzon, I., and Phan, K.L. (2003). Brain-imaging studies of posttraumatic stress disorder. CNS Spectr. *8*, 641–650.

Liu, Y., Rodenkirch, C., Moskowitz, N., Schriver, B., and Wang, Q. (2017). Dynamic Lateralization of Pupil Dilation Evoked by Locus Coeruleus Activation Results from Sympathetic, Not Parasympathetic, Contributions. Cell Rep. *20*, 3099–3112.

Lohani, S., Poplawsky, A.J., Kim, S.G., and Moghaddam, B. (2017). Unexpected global impact of VTA dopamine neuron activation as measured by opto-fMRI. Mol. Psychiatry *22*, 585–594.

Magalhães, R., Barrière, D.A., Novais, A., Marques, F., Marques, P., Cerqueira, J., Sousa, J.C., Cachia, A., and Boumezbeur, F. (2018). The dynamics of stress : a longitudinal MRI study of rat brain structure and connectome. Mol. Psychiatry *23*, 1998–2006.

Mana, M.J., and Grace, A.A. (1997). Chronic cold stress alters the basal and evoked electrophysiological activity of rat locus coeruleus neurons. Neuroscience *81*, 1055–1064.

Manaye, K.F., McIntire, D.D., Mann, D.M.A., and German, D.C. (1995). Locus coeruleus cell loss in the aging human brain: a non-random process. J. Comp. Neurol. *358*, 79–87.

Markicevic, M., Fulcher, B.D., Lewis, C., Helmchen, F., Rudin, M., Zerbi, V., Wenderoth, N., Marija, A., Fulcher, B.D., Lewis, C., et al. (2018). Cortical excitation:inhibition imbalance causes network specific functional hypoconnectivity: a DREADD-fMRI study. bioRxiv. https://doi.org/10.1101/492108.

Mason, S.T., and Fibiger, H.C. (1979). Regional topography within noradrenergic locus coeruleus as revealed by retrograde transport of horseradish peroxidase. J. Comp. Neurol. *187*, 703–724.

Mather, M., Clewett, D., Sakaki, M., and Harley, C.W. (2016). Norepinephrine ignites local hotspots of neuronal excitation: How arousal amplifies selectivity in perception and memory. Behav. Brain Sci. *39*, e200.

McCall, J.G., Al-Hasani, R., Siuda, E.R., Hong, D.Y., Norris, A.J., Ford, C.P., and Bruchas, M.R. (2015). CRH Engagement of the Locus Coeruleus Noradrenergic System Mediates Stress-Induced Anxiety. Neuron *87*, 605–620.

McCall, J.G., Siuda, E.R., Bhatti, D.L., Lawson, L.A., McElligott, Z.A., Stuber, G.D., and Bruchas, M.R. (2017). Locus coeruleus to basolateral amygdala noradrenergic projections promote anxiety-like behavior. eLife *6*, e18247, https://doi.org/10.7554/eLife.18247.

Mulvey, B., Bhatti, D.L., Gyawali, S., Lake, A.M., Kriaucionis, S., Ford, C.P., Bruchas, M.R., Heintz, N., and Dougherty, J.D. (2018). Molecular and Functional Sex Differences of Noradrenergic Neurons in the Mouse Locus Coeruleus. Cell Rep. *23*, 2225–2235.

Murphy, P.R., O'Connell, R.G., O'Sullivan, M., Robertson, I.H., and Balsters, J.H. (2014). Pupil diameter covaries with BOLD activity in human locus coeruleus. Hum. Brain Mapp. *35*, 4140–4154.

Naegeli, C., Zeffiro, T., Piccirelli, M., Jaillard, A., Weilenmann, A., Hassanpour, K., Schick, M., Rufer, M., Orr, S.P., and Mueller-Pfeiffer, C. (2018). Locus Coeruleus Activity Mediates Hyperresponsiveness in Posttraumatic Stress Disorder. Biol. Psychiatry *83*, 254–262.

Ng, L., Bernard, A., Lau, C., Overly, C.C., Dong, H.W., Kuan, C., Pathak, S., Sunkin, S.M., Dang, C., Bohland, J.W., et al. (2009). An anatomic gene expression atlas of the adult mouse brain. Nat. Neurosci. *12*, 356–362.

Nicholas, A.P., Hökfelt, T., and Pieribone, V.A. (1996). The distribution and significance of CNS adrenoceptors examined with in situ hybridization. Trends Pharmacol. Sci. *17*, 245–255.

Palacios, J.M., and Kuhar, M.J. (1980). Beta-adrenergic-receptor localization by light microscopic autoradiography. Science *208*, 1378–1380.

Parlato, R., Otto, C., Begus, Y., Stotz, S., and Schütz, G. (2007). Specific ablation of the transcription factor CREB in sympathetic neurons surprisingly protects against developmentally regulated apoptosis. Development *134*, 1663–1670.

Paschalis, A., Churchill, L., Marina, N., Kasymov, V., Gourine, A., and Ackland, G. (2009). β1-Adrenoceptor distribution in the rat brain: an immunohistochemical study. Neurosci. Lett. *458*, 84–88.

Pietrzak, R.H., Gallezot, J.D., Ding, Y.S., Henry, S., Potenza, M.N., Southwick, S.M., Krystal, J.H., Carson, R.E., and Neumeister, A. (2013). Association of posttraumatic stress disorder with reduced in vivo norepinephrine transporter availability in the locus coeruleus. JAMA Psychiatry *70*, 1199–1205.

Pisani, A., Bonsi, P., Centonze, D., Martorana, A., Fusco, F., Sancesario, G., De Persis, C., Bernardi, G., and Calabresi, P. (2003). Activation of beta1-adrenoceptors excites striatal cholinergic interneurons through a cAMP-dependent, protein kinase-independent pathway. J. Neurosci. *23*, 5272–5282.

Preller, K.H., Burt, J.B., Ji, J.L., Schleifer, C.H., Adkinson, B.D., Stämpfli, P., Seifritz, E., Repovs, G., Krystal, J.H., Murray, J.D., et al. (2018). Changes in global and thalamic brain connectivity in LSD-induced altered states of consciousness are attributable to the 5-HT2A receptor. eLife *7*, e35082.

Ramos, B.P., and Arnsten, A.F.T. (2007). Adrenergic pharmacology and cognition: focus on the prefrontal cortex. Pharmacol. Ther. *113*, 523–536.

Ramos, B.P., Colgan, L., Nou, E., Ovadia, S., Wilson, S.R., and Arnsten, A.F.T. (2005). The beta-1 adrenergic antagonist, betaxolol, improves working memory performance in rats and monkeys. Biol. Psychiatry *58*, 894–900.

Ramos, B.P., Colgan, L.A., Nou, E., and Arnsten, A.F.T. (2008). Beta2 adrenergic agonist, clenbuterol, enhances working memory performance in aging animals. Neurobiol. Aging *29*, 1060–1069.

Reimer, J., McGinley, M.J., Liu, Y., Rodenkirch, C., Wang, Q., McCormick, D.A., and Tolias, A.S. (2016). Pupil fluctuations track rapid changes in adrenergic and cholinergic activity in cortex. Nat. Commun. *7*, 13289.

Reisine, T.D., Nagy, J.I., Beaumont, K., Fibiger, H.C., and Yamamura, H.I. (1979). The localization of receptor binding sites in the substantia nigra and striatum of the rat. Brain Res. *177*, 241–252.

Roeder, T. (2005). Tyramine and octopamine: ruling behavior and metabolism. Annu. Rev. Entomol. *50*, 447–477.

Roelofs, T.J.M., Verharen, J.P.H., van Tilborg, G.A.F., Boekhoudt, L., van der Toorn, A., de Jong, J.W., Luijendijk, M.C.M., Otte, W.M., Adan, R.A.H., and Dijkhuizen, R.M. (2017). A novel approach to map induced activation of neuronal networks using chemogenetics and functional neuroimaging in rats: A proof-of-concept study on the mesocorticolimbic system. Neuroimage *156*, 109–118.

Rommelfanger, K.S., Mitrano, D.A., Smith, Y., and Weinshenker, D. (2009). Light and electron microscopic localization of alpha-1 adrenergic receptor immunoreactivity in the rat striatum and ventral midbrain. Neuroscience *158*, 1530–1540.

Rosazza, C., and Minati, L. (2011). Resting-state brain networks: literature review and clinical applications. Neurol. Sci. *32*, 773–785.

Roth, B.L. (2016). DREADDs for Neuroscientists. Neuron *89*, 683–694.

Rubinov, M., Ypma, R.J.F., Watson, C., and Bullmore, E.T. (2015). Wiring cost and topological participation of the mouse brain connectome. Proc. Natl. Acad. Sci. USA *112*, 10032–10037.

Sara, S.J., and Bouret, S. (2012). Orienting and reorienting: the locus coeruleus mediates cognition through arousal. Neuron *76*, 130–141.

Schallert, T., Whishaw, I.Q., Ramirez, V.D., and Teitelbaum, P. (1978). 6-hydroxydopamine and anticholinergic drugs. Science *202*, 1216–1217.

Schindelin, J., Arganda-Carreras, I., Frise, E., Kaynig, V., Longair, M., Pietzsch, T., Preibisch, S., Rueden, C., Saalfeld, S., Schmid, B., et al. (2012). Fiji: an open-source platform for biological-image analysis. Nat. Methods *9*, 676–682.

Schneider, C.A., Rasband, W.S., and Eliceiri, K.W. (2012). NIH Image to ImageJ: 25 years of image analysis. Nat. Methods *9*, 671–675.

Schroeter, S., Apparsundaram, S., Wiley, R.G., Miner, L.H., Sesack, S.R., and Blakely, R.D. (2000). Immunolocalization of the cocaine- and antidepressant-sensitive l-norepinephrine transporter. J. Comp. Neurol. *420*, 211–232.

Schwarz, L.A., and Luo, L. (2015). Organization of the locus coeruleus-norepinephrine system. Curr. Biol. *25*, R1051–R1056.

Seeley, W.W., Menon, V., Schatzberg, A.F., Keller, J., Glover, G.H., Kenna, H., Reiss, A.L., and Greicius, M.D. (2007). Dissociable intrinsic connectivity networks for salience processing and executive control. J. Neurosci. *27*, 2349–2356.

Seo, D., Jia, Z., Lacadie, C.M., Tsou, K.A., Bergquist, K., and Sinha, R. (2011). Sex differences in neural responses to stress and alcohol context cues. Hum. Brain Mapp. *32*, 1998–2013.

Shine, J.M., Bissett, P.G., Bell, P.T., Koyejo, O., Balsters, J.H., Gorgolewski, K.J., Moodie, C.A., and Poldrack, R.A. (2016). The Dynamics of Functional Brain Networks: Integrated Network States during Cognitive Task Performance. Neuron *92*, 544–554.

Shine, J.M., Breakspear, M., Bell, P.T., Ehgoetz Martens, K.A., Shine, R., Koyejo, O., Sporns, O., and Poldrack, R.A. (2019). Human cognition involves the dynamic integration of neural activity and neuromodulatory systems. Nat. Neurosci. *22*, 289–296.

Sinha, R., Lacadie, C., Skudlarski, P., and Wexler, B.E. (2004). Neural circuits underlying emotional distress in humans. Ann. N Y Acad. Sci. *1032*, 254–257.

Smith, C.C., and Greene, R.W. (2012). CNS dopamine transmission mediated by noradrenergic innervation. J. Neurosci. *32*, 6072–6080.

Sturman, O., Germain, P.L., and Bohacek, J. (2018). Exploratory rearing: a context- and stress-sensitive behavior recorded in the open-field test. Stress *21*, 443–452.

Swanson, L.W., and Hartman, B.K. (1975). The central adrenergic system. An immunofluorescence study of the location of cell bodies and their efferent connections in the rat utilizing dopamine-beta-hydroxylase as a marker. J. Comp. Neurol. *163*, 467–505.

Takeuchi, T., Duszkiewicz, A.J., Sonneborn, A., Spooner, P.A., Yamasaki, M., Watanabe, M., Smith, C.C., Fernández, G., Deisseroth, K., Greene, R.W., and Morris, R.G. (2016). Locus coeruleus and dopaminergic consolidation of everyday memory. Nature *537*, 357–362.

Tervo, D.G.R., Hwang, B.Y., Viswanathan, S., Gaj, T., Lavzin, M., Ritola, K.D., Lindo, S., Michael, S., Kuleshova, E., Ojala, D., et al. (2016). A Designer AAV Variant Permits Efficient Retrograde Access to Projection Neurons. Neuron *92*, 372–382.

Totah, N.K., Neves, R.M., Panzeri, S., Logothetis, N.K., and Eschenko, O. (2018). The Locus Coeruleus Is a Complex and Differentiated Neuromodulatory System. Neuron *99*, 1055–1068.e6.

Totah, N.K.B., Logothetis, N.K., and Eschenko, O. (2019). Noradrenergic ensemble-based modulation of cognition over multiple timescales. Brain Res. *1709*, 50–66.

Uematsu, A., Tan, B.Z., Ycu, E.A., Cuevas, J.S., Koivumaa, J., Junyent, F., Kremer, E.J., Witten, I.B., Deisseroth, K., and Johansen, J.P. (2017). Modular organization of the brainstem noradrenaline system coordinates opposing learning states. Nat. Neurosci. *20*, 1602–1611.

Usher, M., Cohen, J.D., Servan-Schreiber, D., Rajkowski, J., and Aston-Jones, G. (1999). The role of locus coeruleus in the regulation of cognitive performance. Science *283*, 549–554.

Vaisvaser, S., Lin, T., Admon, R., Podlipsky, I., Greenman, Y., Stern, N., Fruchter, E., Wald, I., Pine, D.S., Tarrasch, R., et al. (2013). Neural traces of stress: cortisol related sustained enhancement of amygdala-hippocampal functional connectivity. Front. Hum. Neurosci. *7*, 313.

Valentino, R.J., and Van Bockstaele, E. (2008). Convergent regulation of locus coeruleus activity as an adaptive response to stress. Eur. J. Pharmacol. *583*, 194–203.

Van Dam, D., Vermeiren, Y., Aerts, T., and De Deyn, P.P. (2014). Novel and sensitive reversed-phase high-pressure liquid chromatography method with electrochemical detection for the simultaneous and fast determination of eight biogenic amines and metabolites in human brain tissue. J. Chromatogr. A *1353*, 28–39.

van den Heuvel, M.P., and Hulshoff Pol, H.E. (2010). Exploring the brain network: a review on resting-state fMRI functional connectivity. Eur. Neuropsychopharmacol. *20*, 519–534.

van Marle, H.J.F., Hermans, E.J., Qin, S., and Fernández, G. (2010). Enhanced resting-state connectivity of amygdala in the immediate aftermath of acute psychological stress. Neuroimage *53*, 348–354.

van Oort, J., Tendolkar, I., Hermans, E.J., Mulders, P.C., Beckmann, C.F., Schene, A.H., Fernández, G., and van Eijndhoven, P.F. (2017). How the brain connects in response to acute stress: A review at the human brain systems level. Neurosci. Biobehav. Rev. *83*, 281–297.

Vermeiren, Y., and De Deyn, P.P. (2017). Targeting the norepinephrinergic system in Parkinson's disease and related disorders: The locus coeruleus story. Neurochem. Int. *102*, 22–32.

Weinshenker, D. (2018). Long Road to Ruin: Noradrenergic Dysfunction in Neurodegenerative Disease. Trends Neurosci. *41*, 211–223.

Yang, G.J., Murray, J.D., Wang, X.J., Glahn, D.C., Pearlson, G.D., Repovs, G., Krystal, J.H., and Anticevic, A. (2016). Functional hierarchy underlies preferential connectivity disturbances in schizophrenia. Proc. Natl. Acad. Sci. USA *113*, E219–E228.

Zeiss, C.J. (2005). Neuroanatomical phenotyping in the mouse: the dopaminergic system. Vet. Pathol. *42*, 753–773.

Zerbi, V., Grandjean, J., Rudin, M., and Wenderoth, N. (2015). Mapping the mouse brain with rs-fMRI: An optimized pipeline for functional network identification. Neuroimage *123*, 11–21.

Zerbi, V., Ielacqua, G.D., Markicevic, M., Haberl, M.G., Ellisman, M.H., A-Bhaskaran, A., Frick, A., Rudin, M., and Wenderoth, N. (2018). Dysfunctional Autism Risk Genes Cause Circuit-Specific Connectivity Deficits With Distinct Developmental Trajectories. Cereb. Cortex *28*, 2495–2506.

Zuo, X.N., Kelly, C., Adelstein, J.S., Klein, D.F., Castellanos, F.X., and Milham, M.P. (2010). Reliable intrinsic connectivity networks: test-retest evaluation using ICA and dual regression approach. Neuroimage *49*, 2163–2177.

STAR★METHODS

KEY RESOURCES TABLE

REAGENT or RESOURCE	SOURCE	IDENTIFIER
Antibodies		
Rabbit anti-mCherry	Abcam	Cat#ab167453; RRID: AB_2571870
Mouse anti-TH	ImmunoStar	Cat#22941; RRID: AB_572268
Rabbit anti-cFos	Synaptic Systems	Cat#226 003; RRID: AB_2231974
Mouse anti-NET	Novus Biologicals	Cat#NBP1-28665; RRID: AB_1914141
Chicken anti-GFP	Abcam	Cat#ab13970; RRID: AB_300798
Goat anti-rabbit Alexa 546	Thermo Fisher Scientific	Cat#A-11035; RRID: AB_2534093
Goat anti-mouse Alexa 488	Abcam	Cat#ab150113; RRID: AB_2576208
Goat anti-mouse Cy3	Jackson ImmunoResearch Labs	Cat#115-165-003; RRID: AB_2338680
Goat anti-rabbit Alexa Fluor 488	Thermo Fisher Scientific	Cat#A-11008; RRID: AB_143165
Goat anti-chicken Alexa Fluor 488	Thermo Fisher Scientific	Cat#A-11039; RRID: AB_2534096
NeuroTrace 640/660 Nissl stain	Thermo Fisher Scientific	Cat#N21483; RRID: AB_2572212
Bacterial and Virus Strains		
AAV-5/2-hSyn1-DIO-hM3D(Gq)_mCherry(rev)	Viral Vector Facility (VVF)	VVF Repository: v89-5
AAV-5/2-hSyn1-DIO-mCherry(rev)	Viral Vector Facility (VVF)	VVF Repository: v116-5
AAV-retro/2-hEF1a-DIO-EGFP(rev)	Viral Vector Facility (VVF)	VVF Repository: v217-retro
Chemicals, Peptides, and Recombinant Proteins		
Clozapine	Sigma-Aldrich	Cat#C6305
Medetomidine	Orion Pharma	Swissmedic# 50590
pancuronium bromide	Sigma-Aldrich	Cat#P1918
Isoflurane (Attane)	Piramal Healthcare Limited, India	Swissmedic #56761
Deposited Data		
Allen Reference Atlas	http://mouse.brain-map.org/static/atlas	RRID:SCR_013286
Allen Mouse Brain Atlas (AMBA)	http://mouse.brain-map.org/	RRID:SCR_002978
Experimental Models: Organisms/Strains		
Mouse: C57BL/6-Tg(Dbh-icre)1Gsc	Parlato et al., 2007, Laboratory of Prof. Günther Schütz	MGI:4355551
Software and Algorithms		
ImageJ	Schneider et al., 2012	RRID:SCR_003070
MATLAB	MathWorks	RRID:SCR_001622
FSL	Analysis Group, FMRIB, Oxford, UK	RRID:SCR_002823
ANTS (Advanced Normalization ToolS)	http://picsl.upenn.edu/software/ants/	RRID:SCR_004757

LEAD CONTACT AND MATERIALS AVAILABILITY

Further information and requests for resources and reagents should be directed to and will be fulfilled by the Lead Contact, Johannes Bohacek (johannes.bohacek@hest.ethz.ch).

EXPERIMENTAL MODEL AND SUBJECT DETAILS

All experiments were conducted in accordance with the Swiss federal guidelines for the use of animals in research, and under licensing from the Zürich Cantonal veterinary office. Heterozygous C57BL/6-Tg(Dbh-icre)1Gsc mice (Parlato et al., 2007) were generously provided by Prof. Günther Schütz and kept in breeding trios with wild-type C57BL/6J mice at the ETH Zurich animal facility (EPIC). Experiments were performed with heterozygous or wild-type healthy adult male and female mice that were maintained in IVC cages with food and water *ad libitum*, in a temperature- and humidity-controlled facility on a 12-hour reversed light-dark cycle

(lights off: 9:15am; lights on: 9:15pm) and were housed in groups of 2-5 mice per cage. The behavioral effects of LC activation were first investigated in male and then reproduced and further characterized in female mice (Figure 1 and Figure S1). However the experiments on males and females were performed on separate days to avoid interference of odor cues. Thus, the results of males and females cannot be directly compared to investigate potential sex differences, although the response in both sexes looks very similar. The experimenters were blind to the DREADD groups for all experiments, and all trials were randomized.

METHOD DETAILS

Stereotaxic brain injections

Viral vectors and viral vector plasmids were designed and produced by the Viral Vector Facility (VVF) of the Neuroscience Center Zurich. The viruses used had a physical titer of 6.0-6.5 × 10^{12} vg/ml. For virus delivery, 2- to 3-month-old mice were subjected to stereotactic brain injections. The mice were anesthetized with isoflurane and placed in a stereotaxic frame. For analgesia, animals received a subcutaneous injection of 2 mg/kg Meloxicam and a local anesthetic (Emla cream; 5% lidocaine, 5% prilocaine) before and after surgery. A pneumatic injector (Narishige, IM-11-2) and calibrated microcapillaries (Sigma-Aldrich, P0549) were used to inject 1 μL of virus (either ssAAV-5/2-hSyn1-dlox-hM3D(Gq)_mCherry(rev)-dlox-WPRE-hGHp(A) or ssAAV-5/2-hSyn1-dlox-mCherry(rev)-dlox-WPRE-hGHp(A)) bilaterally into the locus coeruleus (coordinates from bregma: anterior/posterior −5.4 mm, medial/lateral ± 1.0 mm, dorsal/ventral −3.8 mm). For the retrograde AAV2 injection, 0.8 μL of ssAAV-retro/2-hEF1α-dlox-hChR2(H134R)_mCherry(rev)-dlox-WPRE-hGHp(A) or ssAAV-retro/2-hEF1a-dlox-EGFP(rev)-dlox-WPRE-bGHp(A) was delivered bilaterally to the dorsolateral site of the caudate-putamen (from bregma: anterior/posterior 0.86 mm, medial/lateral ± 1.8 mm, dorsal/ventral −3.2 mm). The health of the animals was evaluated by post-operative checks over the course of 3 consecutive days.

Pupil recordings

For pupil recordings we used a Raspberry Pi NoIR Camera Module V2 night vision camera, an infrared light source (Pi Supply Bright Pi - Bright White and IR camera light for Raspberry Pi) and a Raspberry Pi 3 Model B (Raspberry Pi Foundation, UK). Animals were anesthetized with isoflurane (4% induction, 1.5% maintenance), then an intraperitoneal catheter delivering PBS was placed and the video recording was initiated. After 2 minutes of baseline recording, 0.03 mg/kg clozapine (Sigma-Aldrich, Steinheim, Germany) was injected through the catheter and the video recording continued for another 8 minutes.

Behavioral testing

All experiments took place in testing rooms illuminated with red LED lights (637 nm), during the dark period of the light-dark cycle.

Open field test (OFT)

Open-field testing took place inside sound insulated, ventilated multi-conditioning chambers (MultiConditioning System, TSE Systems Ltd, Germany). The open field arena (45 cm (l) x 45 cm (w) x 40 cm (h)) consisted of four transparent Plexiglas walls and a light gray PVC floor. Mice were tested under dim lighting (4 Lux across the floor of the open field, provided by four equally spaced yellow overhead lights) with 75-77 dB of white noise playing through the speakers of each box, as described previously (Sturman et al., 2018). Animals were injected i.p. with 0.03 mg/kg clozapine (Sigma-Aldrich, Steinheim, Germany) and placed directly into the center of the open field. Tracking/recording was initiated upon first locomotion grid beam break, lasted for 30 minutes and was analyzed in 3-minute bins.

Light dark box (LDB)

For the light dark box testing, a box with a light and a dark compartment was placed inside sound insulated, ventilated multi-conditioning chambers (MultiConditioning System, TSE Systems Ltd, Germany). The light dark compartment (28cm (l) x 30 cm (w) x 25 cm (h)) consisted of transparent Plexiglas walls, while the dark compartment (16cm (l) x 30 cm (w) x 25 cm (h)) with black Plexiglas walls. The compartments were separated with a black Plexiglas dividing wall with a small central opening (6.6cm (w) x 7cm (h)) to let the mouse move freely between compartments. The entire arena had a light gray PVC floor. Two white lights directly above the light compartment were used to light the arena (200 Lux in the light compartment, 0-1 lux in the dark compartment). 60-65 dB of white noise was played through the speakers of each box throughout testing. Animals were injected i.p. with 0.03 mg/kg clozapine (Sigma-Aldrich, Steinheim, Germany) and placed directly into the center of the light compartment. Tracking/recording was initiated upon first locomotion grid beam break, lasted for 30 minutes and was analyzed in 3-minute bins.

Rotarod test

To test motor function of mice during chemogenetic actication of LC, we tested them on a Rotarod (Accurotor Rota Rod, Accuscan Instruments, Inc.) accelerating from 4 to 40 rpm in 300 s. Mice were subjected in 5 trials/day for 3 consecutive days. The maximum duration of every trial was 5 minutes, and minimum 5 minutes break was given between trials. After a day of training, the mice were tested on the Rotarod on Day 2. On Day 3, all mice were injected with 30 μg/kg clozapine i.p. and immediately placed on the Rotarod.

Tissue collection and processing

Tissue collection for immunohistochemistry

When brain tissue was collected exclusively for immunohistochemistry, mice were deeply anesthetized with pentobarbital (150 mg/kg, i.p.) and perfused intracardially through the left ventricle for 2 minutes, with approximately 20 mL ice-cold PBS

(pH 7.4). The brain was dissected, blocked and fixed for 2-3 hr in ice-cold paraformaldehyde solution (4% PFA in PBS, pH 7.4). The tissue was rinsed with PBS and stored in a sucrose solution (30% sucrose in PBS) at 4°C, overnight. Then the tissue was frozen in tissue mounting medium (Tissue-Tek O.C.T Compound, Sakura Finetek Europe B.V., Netherlands), and sectioned coronally using a cryostat (Leica CM3050 S, Leica Biosystems Nussloch GmbH) into 40 μm thick sections. The sections were immediately transferred into ice-cold PBS.

Tissue collection for uHPLC and immunohistochemistry

When brain tissue was collected for both uHPLC and immunohistochemistry, mice were rapidly euthanized by cervical dislocation. The brain was first divided into an anterior and a posterior part with a single cut from a razorblade at the beginning of the cerebellum as shown in Figure 5A. The cortex (overlying the hippocampus), hippocampus and striatum were immediately dissected on an ice-cold glass surface, snap-frozen in liquid nitrogen and stored at −80°C until further processing for uHPLC. The posterior part including the locus coeruleus was fixed in 4% PFA for 2 hours, cryoprotected in a sucrose solution and frozen in mounting medium as described above for immunohistochemistry.

Brain illustrations were created with the Scalable Brain Atlas (Bakker et al., 2015; Lein et al., 2007).

Immunohistochemistry

For immunohistochemistry, brain sections were submerged in primary antibody solution containing 0.2% Triton X-100, and 2% normal goat serum in PBS, and were incubated at 4°C under continuous agitation over 2 nights. Then the sections were washed 3 times in PBS for 10 minutes/wash, and transferred in secondary antibody solution containing 2% normal goat serum in PBS. After 3 more PBS washes, the sections were mounted onto glass slides (Menzel-Gläser SUPERFROST PLUS, Thermo Scientific), air-dried and coverslipped with Dako fluorescence mounting medium (Agilent Technologies). The primary antibodies used were: rabbit anti-mCherry (ab167453, Abcam, 1:1000), mouse anti-TH (22941, Immunostar, 1:1000), rabbit anti-cFOS (226 003, Synaptic Systems, 1:5000), mouse anti-NET (NBP1-28665, Novus Biologicals, 1:1000), chicken anti-GFP (ab13970, Abcam. 1:1000). The secondary antibodies used were: goat anti-rabbit Alexa 546 (A11035, Thermo Fisher Scientific, 1:300), goat anti-mouse Alexa 488 (ab150113, Abcam, 1:300), goat anti-mouse Cy3 (115-165-003, Jackson ImmunoResearch, 1:300), goat anti-rabbit Alexa Fluor 488 (A-11008, Thermo Fisher Scientific, 1:500), goat anti-chicken Alexa Fluor 488 (A-11039, Thermo Fischer Scientific, 1:1000) and Nissl stain (N21483, NeuroTrace 640/660 Nissl stain, Thermo Fischer Scientific, 1:300).

Microscopy images were acquired in a confocal laser-scanning microscope (CLSM 880, Carl Zeiss AG, Germany), maintaining a pinhole aperture of 1.0 Airy Unit and image size 1024x1024 pixels. Images of LC were acquired using a Z stack with a 20x objective and pixel size 0.59 μm. Images of the caudate putamen and the whole brain (sagittal plane) were acquired with the 20x (pixel size 0.59 μm) and the 10x (pixel size 1.19 μm) objective respectively, using a Z stack and tiles. Images of axons were acquired with the 20x (pixel size 0.59 μm) or the 40x (pixel size 0.35 μm) objective.

MRI

Anesthesia

The levels of anesthesia and physiological parameters were monitored to obtain a reliable measurement of functional connectivity following established protocols (Grandjean et al., 2014; Zerbi et al., 2015). Briefly, anesthesia was induced with 4% isoflurane and the animals were endotracheally intubated and the tail vein cannulated. Mice were positioned on a MRI-compatible cradle, and artificially ventilated at 80 breaths per minute, 1:4 O_2 to air ratio, and 1.8 ml/h flow (CWE, Ardmore, USA). A bolus injection of muscle relaxant (pancuronium bromide, 0.2 mg/kg) was administered, and isoflurane was reduced to 1%. Throughout the experiment, mice received a continuous infusion of pancuronium bromide 0.4 mg/kg/h. Body temperature was monitored using a rectal thermometer probe, and maintained at 36.5°C ± 0.5 during the measurements. The preparation of the animals did not exceed 15 minutes. In an additional experiment, mice were pre-treated with a bolus injection of medetomidine 0.05 mg/kg, followed by a continuous infusion at 0.1 mg/kg/h.

Data acquisition

Data acquisition was performed on a Biospec 70/16 small animal MR system (Bruker BioSpin MRI, Ettlingen, Germany) equipped with a cryogenic quadrature surface coil for signal detection (Bruker BioSpin AG, Fällanden, Switzerland). Standard adjustments included the calibration of the reference frequency power and the shim gradients using MapShim (Paravision v6.1). For anatomical assessment, a T2-weighted image is acquired (FLASH sequence, in-plane resolution of 0.05 × 0.02 mm, TE = 3.51, TR = 522ms). For functional connectivity acquisition, a standard gradient-echo echo planar imaging sequence (GE-EPI, repetition time TR = 1 s, echo time TE = 15ms, in-plane resolution RES = 0.22 × 0.2mm^2, number of slice NS = 20, slice thickness ST = 0.4 mm, slice gap = 0.1mm) was applied to acquire 2280 volumes in 38 min. After 15 minutes of GE-EPI acquisition, a bolus of 0.03 mg/kg clozapine was intravenously injected to activate DREADDs.

Outlier Removal

All mice (hM3Dq-mCh n = 11; mCh n = 8) successfully completed both fMRI sessions. However, due to a fault in the ventilation system that artificially supports breathing after the MRI, three animals died after the second session (hM3Dq-mCh n = 2; mCh n = 1). For all the others, the time until conscious intention to move was 10.6 ± 4 minutes. One animal (mCh group) was excluded from the rs-fMRI analysis because the preparation time exceeded 30 minutes (average time between anesthesia induction and start of the MRI

scanning, including intubation and cannulation was 12.8 ± 3 minutes). In the weeks between the second fMRI session and tissue collection for molecular analyses, 2 mice were found dead in their cage (n = 1 from hM3Dq-mCh, and n = 1 from mCh groups). Otherwise, no mice were excluded from any of the experiments.

Ultra-high performance liquid chromatography (uHPLC)

To quantify norepinephrinergic (NE; epinephrine; MHPG), dopaminergic (DA; DOPAC; HVA), and serotonergic (5-HT; 5-HIAA) compounds, a reversed-phase uHPLC system coupled with electrochemical detection (RP-uHPLC-ECD) was used (Alexys™ Neurotransmitter Analyzer, Antec Leyden, Zoeterwoude, Netherlands). In short, our previously validated RP-HPLC method with ion pairing chromatography was applied as described (Van Dam et al., 2014), albeit with minor modifications regarding the installed column (BEH C18 Waters column, 150 mm x 1mm, 1.7μm particle size) and pump preference (LC110S pump, 497 bar; flow rate of 68μL/min), achieving the most optimal separation conditions in a RP-uHPLC setting. Levels of the monoamines and metabolites were calculated using Clarity software™ (DataApex Ltd., v6.2.0.208, 2015, Prague, Czech Republic).

Brain samples were defrosted to 4°C and subsequently homogenized in 800 μL ice-cold sample buffer (50 mM citric acid, 50 mM phosphoric acid, 0.1 mM EDTA, 8 mM KCl and 1.8 mM octane-1-sulfonic acid sodium salt (OSA), adjusted to pH = 3.6), using a Bio-Gen PRO200 homogenizer (PRO Scientific Inc., Oxford, CT, USA; 60 s, 4°C). To remove excess proteins, 450 μL homogenate was transferred onto a 10,000 Da Amicon® Ultra 0.5 Centrifugal Filter (Millipore, Ireland) that had been pre-washed twice using 450 μL sample buffer (centrifugation: 14,000 × g, 20 min, 4°C). The Amicon® filter loaded with the homogenate was then centrifuged (14,000 × g, 20 min, 4°C). Finally, the filtrate was transferred into a polypropylene vial (0.3mL, Machery-Nagel GmbH & Co. KG, Germany) and automatically injected into the previously-mentioned uHPLC column by the Alexys AS110 sample injector.

QUANTIFICATION AND STATISTICAL ANALYSIS

Statistical details for every experiment are provided in the figure legends, where "n" represents number of animals per group. Statistical significance was defined as $p < 0.05$.

Quantification

Pupillometry

Pupil diameter was measured using a custom MATLAB (MathWorks, Natick, MA, USA) script. Frames were binarized and an ellipse-fitting algorithm was used to approximate the pupil size. Measurements after clozapine injection were then normalized to baseline (measurements before clozapine).

OFT and LDB

All output parameters of the OFT and LDB were quantified by the software of the MultiConditioning System (TSE Systems Ltd, Germany).

cFOS expression

Confocal images were imported to ImageJ (Schneider et al., 2012) enabled by Fiji (Schindelin et al., 2012), and neurons (Nissl positive cells) expressing TH, cFOS or both were counted manually.

Statistical analysis

GraphPad Prism 8.0 was used for statistical analyses for behavior, pupillometry, immunohistochemistry and uHPLC data. We used independent samples t tests when comparing two independent groups, and paired-samples t tests when comparing the same group twice. When comparing more than two groups, we used one-way ANOVAs if there was a single independent variable, or two-way ANOVAs for two-factorial designs (e.g., time x group). Significant main effects and interactions were analyzed using Sidak's post hoc tests.

Resting-state fMRI

Data pre-processing and analysis

Resting state fMRI datasets were de-spiked and artifacts were removed using an existing automated pipeline designed in FSL (https://fsl.fmrib.ox.ac.uk/fsl/fslwiki/), adapted for the mouse (Zerbi et al., 2015). This procedure includes ICA-based artifact removal, motion correction and regression. Thereafter, datasets were band-pass filtered (0.01-0.25 Hz), skull-stripped and normalized to the Allen Brain Institute reference atlas (http://mouse.brain-map.org/static/atlas) using ANTs v2.1 (http://picsl.upenn.edu/software/ants/).

Two types of analyses were performed on this data to compare the influence of LC activation on functional connectivity; first, we employed an exploratory and data-driven *connectome* analysis to describe the temporal and spatial changes at the whole-brain level. Briefly, BOLD time series are extracted using a subset of ROIs from the Allen Common Coordinate Framework (V3, http://help.brain-map.org/download/attachments/2818169/MouseCCF.pdf), which consisted of 165 ROIs from isocortex, hippocampal formation, cortical subplate, striatum, pallidum, thalamus, hypothalamus, hindbrain and midbrain (full list available in Table S1). Connectivity couplings between all ROIs are measured using a regularized Pearson's correlation coefficient implemented in FSLNets, using sliding time windows of either 1 minute (Figure 2) or 15 minutes (Figure 3). The connectome matrices were fed

into a nonparametric permutation testing with 5000 permutations to detect differences in edge strength (i.e., connectivity between two brain areas or nodes) between groups. The results were corrected for multiple comparisons with Network Based Statistics (NBS) toolbox, and considered significant at a $p < 0.05$.

In our second analyses, we focused on changes in spatial patterns of correlated activity, also called resting-state networks (RSNs). We selected 15 meaningful RSNs from an independent cohort of n = 15 mice. Please note that the motor network, the striatum network and the striato-motor network are highly correlated, thus we considered only the latter for the analysis and reduced the number of RSNs to 13. We performed a dual regression approach (Zuo et al., 2010) as described by Zerbi et al. (2018). With this approach, we derived an index of coupling strength (i.e., temporal synchronicity) of the voxels within each RSN, by averaging the Z-scores from the group-mean RSNs masks (thresholded at the 75^{th} percentile). Group level statistics were performed in SPSS v22 using a Linear Mixed-Model, with the fixed factors DREADD-Group and Time (2-levels, repeated-measure), and with the individual mice as the random factor. Corresponding contrasts were used for post hoc pairwise comparisons (LSD). *P*-values were considered significant at $p < 0.05$ after False Discovery Rate (FDR) correction for multiple comparisons between RSNs.

Gene expression

Gene expression data were obtained from the Allen Mouse Brain Atlas (AMBA) (Lein et al., 2007) using the Allen Software Development Kit (SDK, https://github.com/benfulcher/AllenSDK) (Fulcher et al., 2019). Gene expression data in the AMBA is measured using *in situ* hybridization from: (i) sagittal section experiments with high genome coverage, and (ii) coronal section replications for approximately 3500 genes with restricted expression patterns in the brain (11). Transcriptional levels of major neurotransmitters across a macroscopic cortical area were summarized as the 'expression energy' (the mean ISH intensity across voxels of that brain area) (Lein et al., 2007; Ng et al., 2009).

Correlation and multiple regression analyses

Correlations between Node Modulation Index and gene expression data were conducted using Spearman's correlations. A null distribution of Spearman's rho values was obtained for each gene by shuffling NMI ROI labels 10.000 times in a MATLAB (MathWorks, Natick, MA, USA) using a script developed in-house. We also used Spearman partial correlation to find the relative importance of each gene subunit influencing NMI correlations. Transcriptional levels of genes within the same families (i.e., adrenergic, dopaminergic, cholinergic nicotinic) were not considered in the regression due to their strong co-expression. See Table S2 for details

DATA AND CODE AVAILABILITY

Resting-state fMRI datasets are available upon request to the authors.

Neuron, Volume *103*

Supplemental Information

Rapid Reconfiguration of the Functional Connectome after Chemogenetic *Locus Coeruleus* Activation

Valerio Zerbi, Amalia Floriou-Servou, Marija Markicevic, Yannick Vermeiren, Oliver Sturman, Mattia Privitera, Lukas von Ziegler, Kim David Ferrari, Bruno Weber, Peter Paul De Deyn, Nicole Wenderoth, and Johannes Bohacek

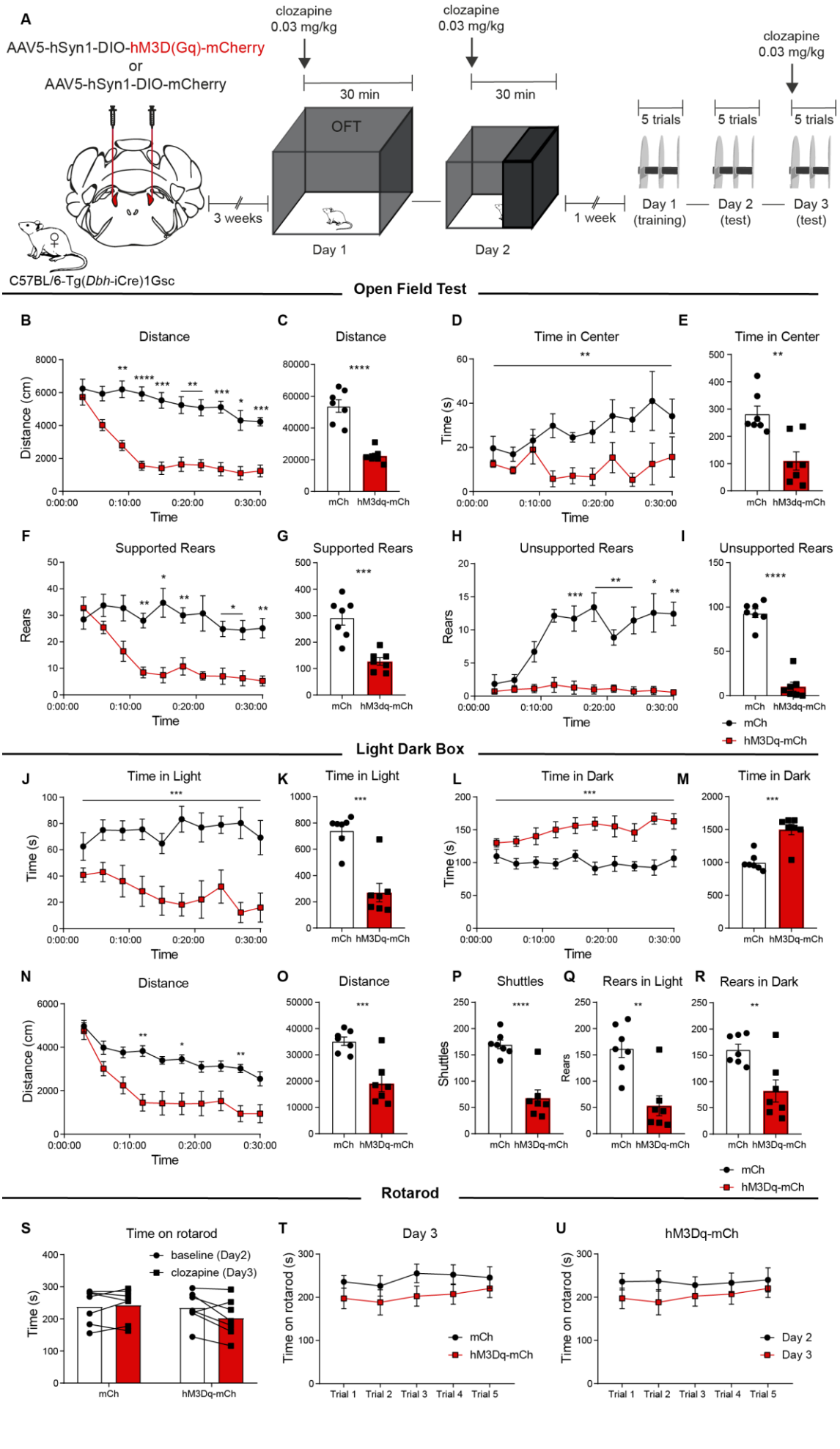
A
AAV5-hSyn1-DIO-hM3D(Gq)-mCherry
or
AAV5-hSyn1-DIO-mCherry
C57BL/6-Tg(Dbh-iCre)1Gsc
3 weeks
clozapine
0.03 mg/kg
30 min
OFT
Day 1
clozapine
0.03 mg/kg
30 min
Day 2
1 week
5 trials
Day 1
(training)
5 trials
Day 2
(test)
clozapine
0.03 mg/kg
5 trials
Day 3
(test)
Open Field Test
B
Distance
Distance (cm)
Time
C
Distance
mCh
hM3dq-mCh
D
Time in Center
Time (s)
Time
E
Time in Center
mCh
hM3dq-mCh
F
Supported Rears
Rears
Time
G
Supported Rears
mCh
hM3dq-mCh
H
Unsupported Rears
Rears
Time
I
Unsupported Rears
mCh
hM3dq-mCh
mCh
hM3Dq-mCh
Light Dark Box
J
Time in Light
Time (s)
Time
K
Time in Light
mCh
hM3Dq-mCh
L
Time in Dark
Time (s)
Time
M
Time in Dark
mCh
hM3Dq-mCh
N
Distance
Distance (cm)
Time
O
Distance
mCh
hM3Dq-mCh
P
Shuttles
Shuttles
mCh
hM3Dq-mCh
Q
Rears in Light
Rears
mCh
hM3Dq-mCh
R
Rears in Dark
mCh
hM3Dq-mCh
mCh
hM3Dq-mCh
Rotarod
S
Time on rotarod
baseline (Day2)
clozapine (Day3)
Time (s)
mCh
hM3Dq-mCh
T
Day 3
Time on rotarod (s)
mCh
hM3Dq-mCh
Trial 1
Trial 2
Trial 3
Trial 4
Trial 5
U
hM3Dq-mCh
Time on rotarod (s)
Day 2
Day 3
Trial 1
Trial 2
Trial 3
Trial 4
Trial 5

Figure S1. Related to Figure 1. (**A**) Diagram showing the time-course of behavioral tests after virus delivery in the LC of female DBH-iCre mice. (**B-I**) Mice were placed in the OFT directly after clozapine injection for 30 minutes. Mice expressing hM3Dq-mCh travelled less distance compared to mice expressing only mCh (**B, C:** main effect of group: $F(1,12)=53.71$, $p<0.0001$, interaction: $F(9,108)=6.32$, $p<0.0001$, two-way ANOVA with Sidak *post hoc* tests), spent less time in the center (**D, E:** main effect of group $F(1,12)=15.81$, $p=0.0018$, two-way ANOVA) and performed fewer supported rears (**F, G:** main effect of group $F(1,12)=27.46$, $p=0.0002$, interaction: $F(9,108)=4.24$, $p=0.0001$, two-way ANOVA with Sidak *post hoc* tests) and unsupported rears (**H, I:** main effect of group: $F(1,12)=137.9$, $p<0.0001$, interaction: $F(9,108)=5.26$, $p<0.0001$, two-way ANOVA with Sidak *post hoc* tests). (**J-R**) Mice were placed in the light dark box directly after clozapine injection for 30 minutes. Mice expressing hM3Dq-mCh spent less time in the light compartment in comparison to mCh controls (**J, K:** main effect of group: $F(1,12)=31.44$, $p=0.0001$, two-way ANOVA), more time in the dark compartment (**L, M:** main effect of group: $F(1,12)=28.75$, $p=0.0002$, two-way ANOVA), and travelled less distance (**N, O:** main effect of group: $F(1,12)=20.65$, $p=0.0007$, interaction: $F(9,108)=2.67$, $p=0.0072$, two-way ANOVA with Sidak *post hoc* tests). (**P-R**) Compared to mCh controls, hM3Dq-mCh mice also performed fewer shuttles between the light and the dark compartment (**P:** $t(12)=5.81$, $p<0.0001$, unpaired t test) and fewer rears in both compartments (**Q:** $t(12)=4.26$, $p=0.0011$, **R:** $t(12)=3.36$, $p=0.0057$, unpaired t test). (**S-U**) To assess gross motor function we trained the same mice on the Rotarod (Day 1, 5 trials) and tested them at baseline (Day 2, 5 trials) and immediately after clozapine injection (Day 3, 5 trials). The average performance from all trials of hM3Dq-mCh mice was slightly lower, not significantly different from mCh controls (**S:** main effect of group: $F(1,12)=2.61$, $p=0.1318$, interaction virus x group: $F(1,12)=4.61$, $p=0.0528$, two-way ANOVA). On Day 3, the performance of hM3Dq-mCh and mCh mice was not significantly different over the course of 5 trials (**T:** main effect of group: $F(1,12)=1.80$, $p=0.2040$, interaction trial x group: $F(4,48)=0.45$, $p=0.7743$, two-way ANOVA) and the performance of hM3Dq-mCh was not different between Day 2 and Day 3 over the course of 5 trials (**U:** main effect of group: $F(1,12)=1.18$, $p=0.2982$, interaction trial x group: $F(4,48)=0.46$, $p=0.7667$). *$p<0.05$, **$p<0.01$, ***$p<0.001$, ****$p<0.0001$. Data represent mean ± SEM

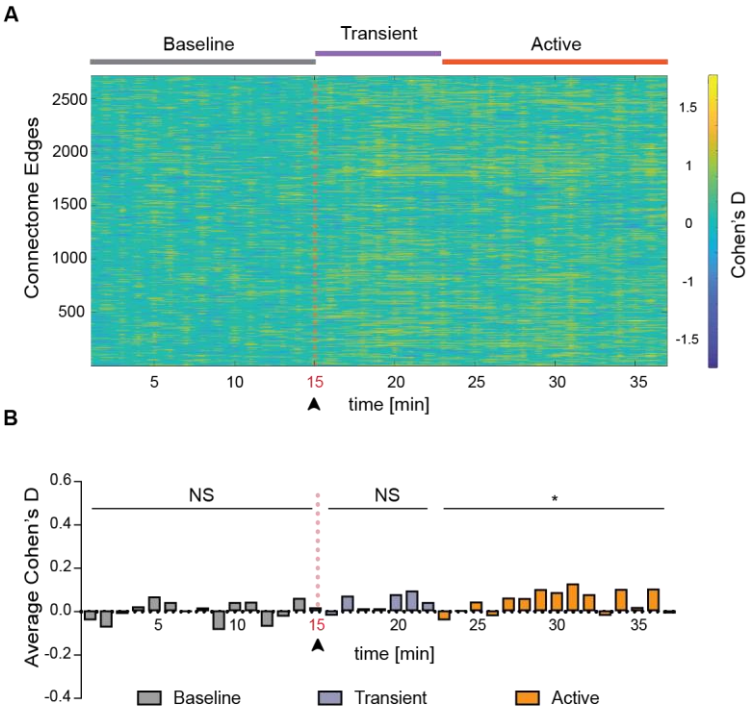

Figure S2. Related to Figure 2. Minor FC changes between anesthesia with 1% isoflurane versus anesthesia with 0.5% isoflurane+medetomidine. Effect-size (Cohen's D) analysis of Functional Connectivity (FC) is shown for single-edges (n=2724) between mCh mice (n=7) under two anesthesia conditions (see methods) (**A**) and for the average across all edges (**B**). The distribution of the data reveals a reduction of connectivity in multiple edges in the "1% isoflurane"-condition compared to the "0.5% isoflurane + medetomidine"-condition, about 30 minutes after the start of the session (Wilcoxon two-tailed test: p=0.9780 for baseline period, p=0.0781 for transient period and p=0.0181 for active period). The average net-effect of anesthesia is approximately 7 times smaller than the effect of LC-NE DREADD activation.

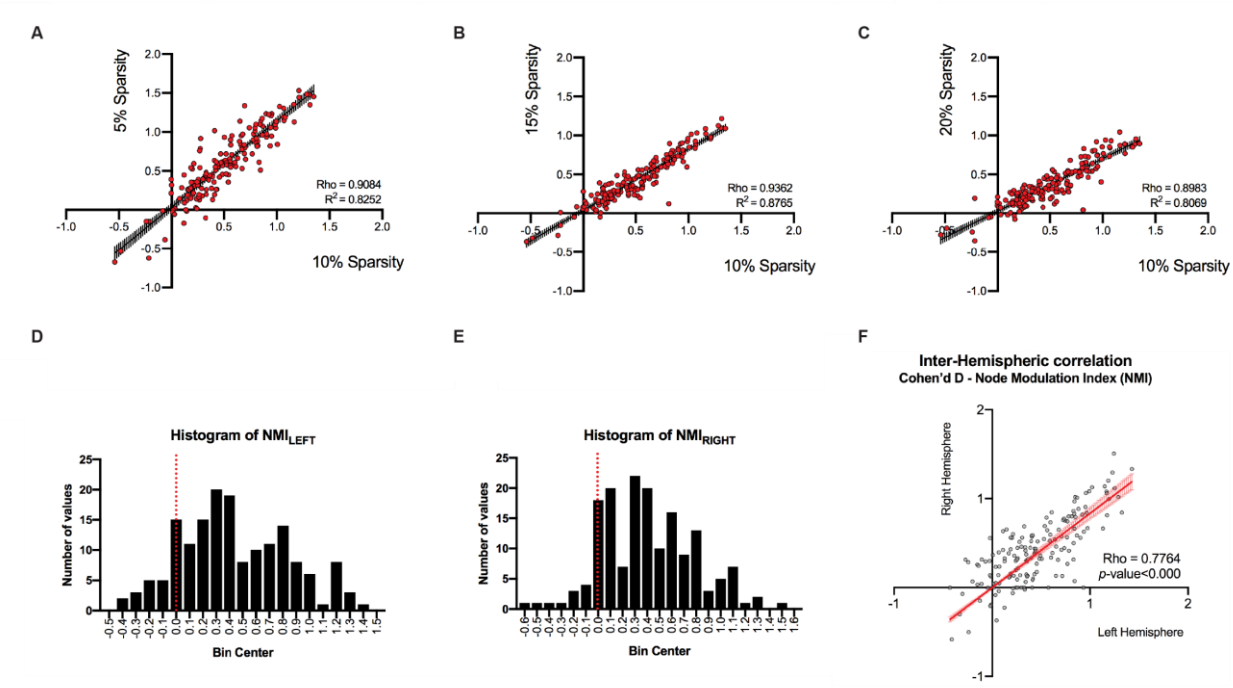

Figure S3. Related to Figure 3. (**A-C**) The Node Modulation Index (NMI) effect size is a robust index and correlates at different connectome sparsity-thresholds. The NMI effect size between mCh (n=7) and hM3Dq-mCh (n=11) under 1% isoflurane anesthesia is calculated at different sparsity thresholds (5%, 15%, 20%) of the connectome matrix. In each case, the resulting indices were highly linearly correlated (Pearson's correlation, *p*-value < 0.0001). (**D-F**) Coherent FC changes in the left and right hemisphere after LC-NE activation. Right-skewed distribution plots of Node Modulation Index effect size (Cohen's D) in the left (**D**) and in the right (**E**) hemispheres, demonstrating hyper-connectivity in both hemispheres. (**F**) The NMI measured in the left hemisphere shows positive linear correlation with respect to right hemisphere NMI (Pearson Rho=0.7764, p<0.0001). Data from mCh (n=7) and hM3Dq-mCh (n=11) under 1% isoflurane anesthesia.

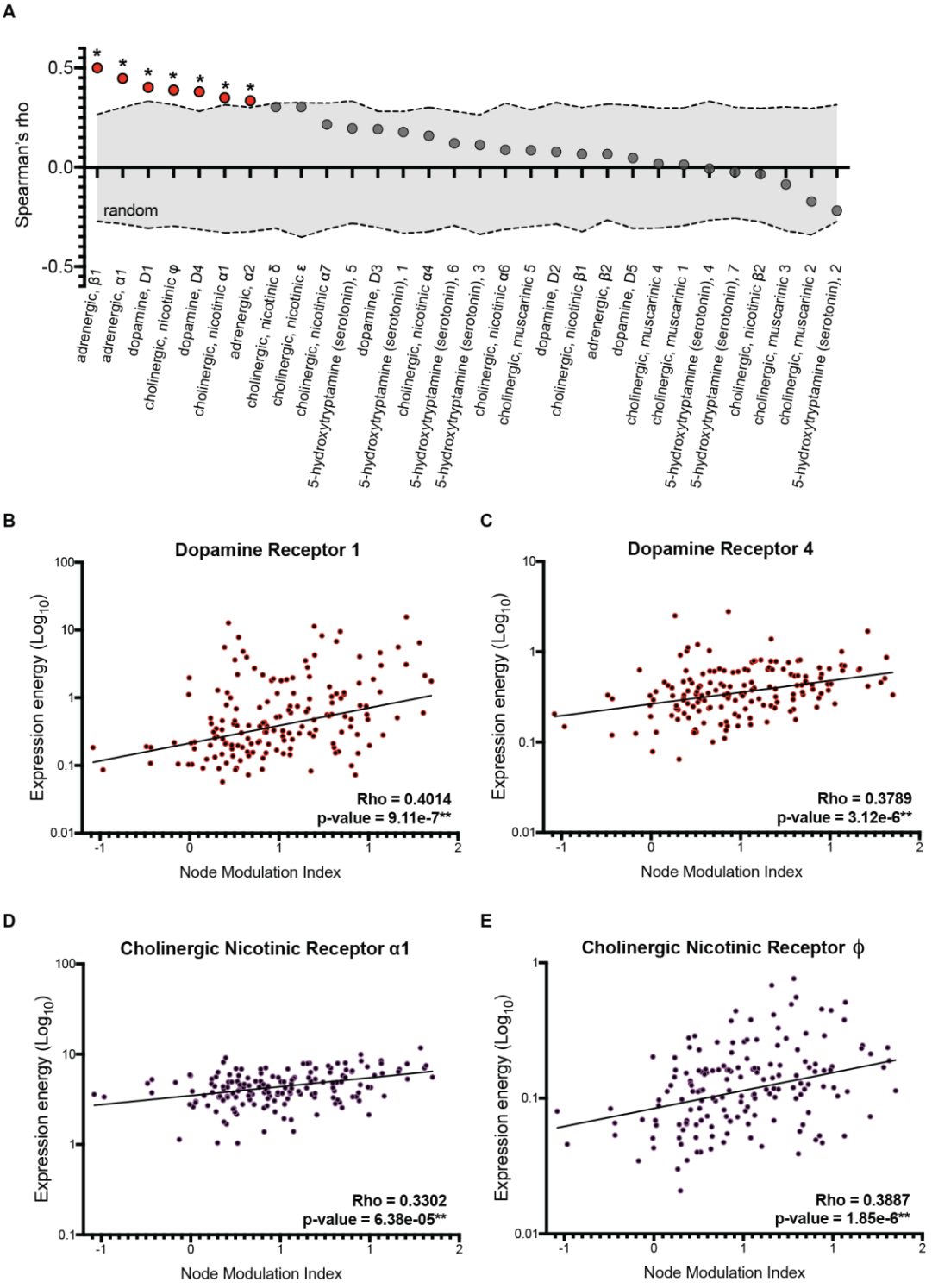

Figure S4. Related to Figure 4. Node Modulation Index maps correlate with dopamine D1, D4 and cholinergic nicotinic Φ and α1 receptor gene-transcript maps. (**A**) Spearman correlation coefficients, Rho, between Node Modulation Index (NMI) and gene-transcript maps for Adrenergic, Cholinergic, Dopaminergic and Serotonergic receptors were compared to a distribution of 100.000 randomized shuffled NMI labels. Whilst the highest correlation was achieved by adrenergic β1 and α1 receptor maps, we found a significant correlation and associated p-value (FDR corrected) between NMI and the transcriptional maps of genes coding dopaminergic receptor subunits 1 and 4 (**B**-**C**) and cholinergic nicotinic Φ and α1 (**D**-**E**). None of the transcriptional maps of cholinergic muscarinic nor serotonin receptors show significant correlation with the NMI.

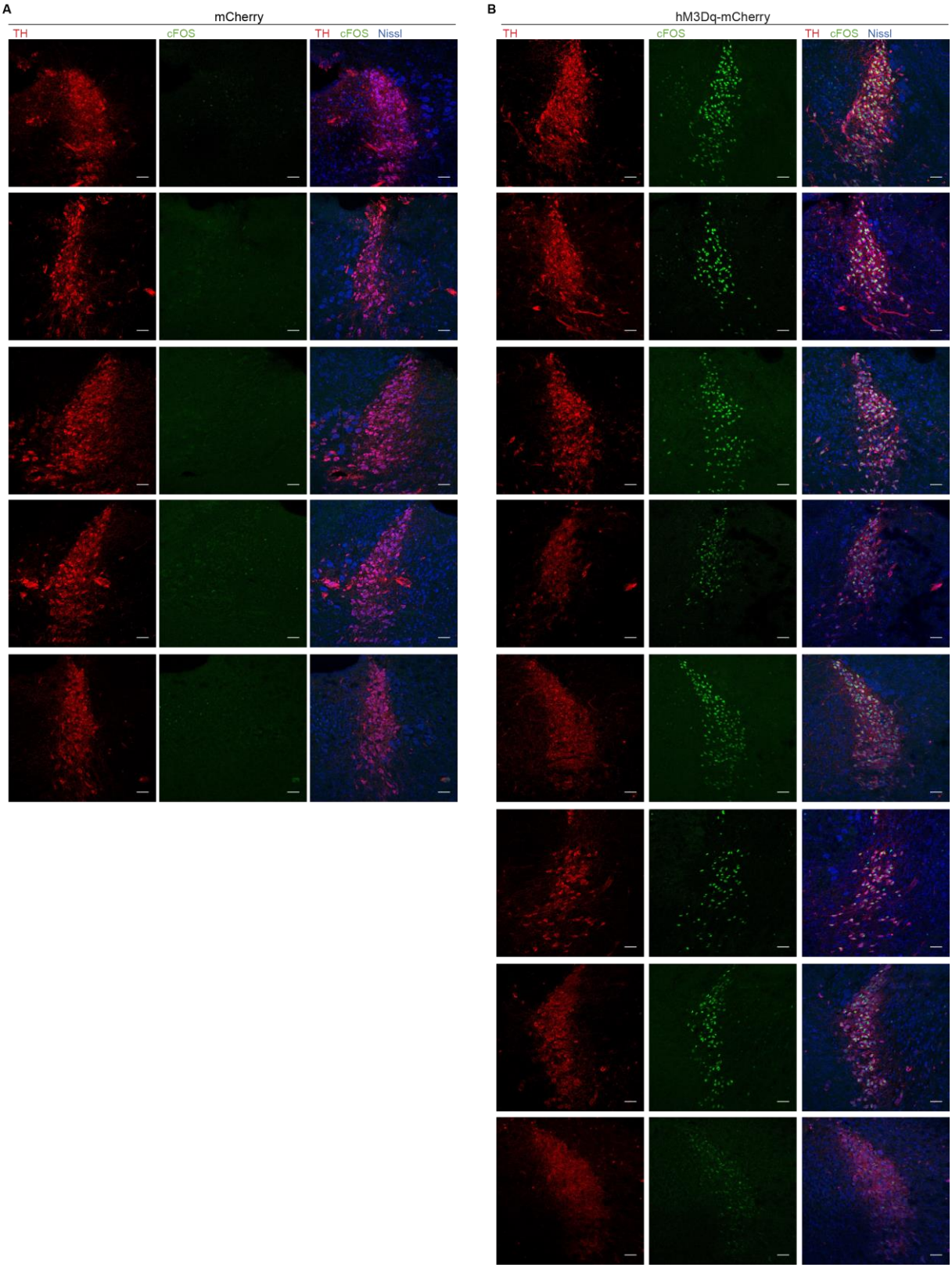

Figure S5. Related to Figure 6. Representative LC images of every mouse used for the fMRI scans. Every row shows 3 images from one mouse, stained for TH (left), cFOS (middle), and the merged picture including a Nissl stain (right). Tissue was collected 90 minutes after 0.03mg/kg clozapine injection, and cFOS is activated in all mice expressing hM3Dq-mCh (**B**), but not in mCh controls (**A**). Tissue collected as described in Figure 6A. All scale bars: 50 μm.

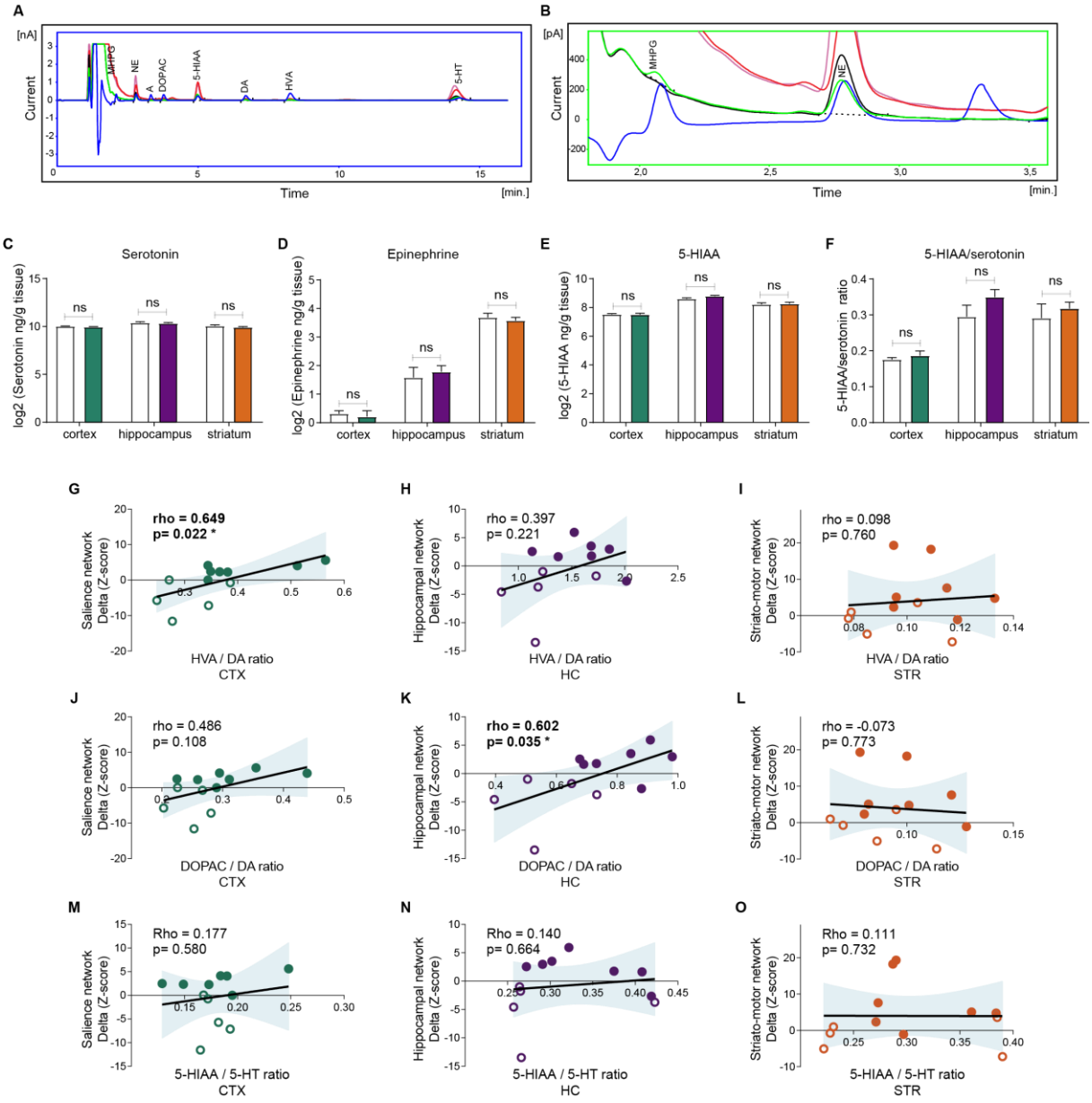

Figure S6. Related to Figure 6. (**A**) uHPLC chromatograms of hippocampus samples from an mCh mouse (undiluted in pink, 3 times diluted in black), an hM3Dq-mCh mouse (undiluted in red, 3 times diluted in green) and the standard (blue). (**B**) Magnification of (**A**) showing the chromatogram from an hM3Dq-mCh mouse with higher MHPG and lower NE values (green) resulting in a high norepinephrine turnover ratio (MHPG/NE), in contrast with the chromatogram from an mCh mouse (black). The standard is in blue. 5-HIAA: 5-hydroxyindoleacetic acid, 5-HT: 5-hydroxytryptamine (serotonin), E: epinephrine, DA: dopamine, DOPAC: 3,4-dihydroxyphenylacetic acid, HVA: homovanillic acid, MHPG: 3-methoxy-4-hydroxyphenylglycol, nA: nanoampere, NE: norepinephrine, pA: picoampere. (**C-F**) Levels of serotonin, epinephrine, 5-HIAA, and serotonin turnover (5-HIAA/serotonin ratio) remained unchanged in response to LC activation. Samples were collected 90 minutes after 0.03 mg/kg clozapine injection (two-way ANOVA), as explained in Figure 6A. Data represent mean ± SEM. (**G-O**) Spearman correlation coefficients Rho, and associated p-value (FDR corrected) between the turnover of DA (**G-L**) and 5-HT (**M-O**) in the cortex, hippocampus and striatum, and the changes in network connectivity in the Salience Network (left), Hippocampal Network (middle), and Striato-Motor Networks (right) respectively. (CTX: cortex, HC: hippocampus, STR: striatum = caudate putamen)

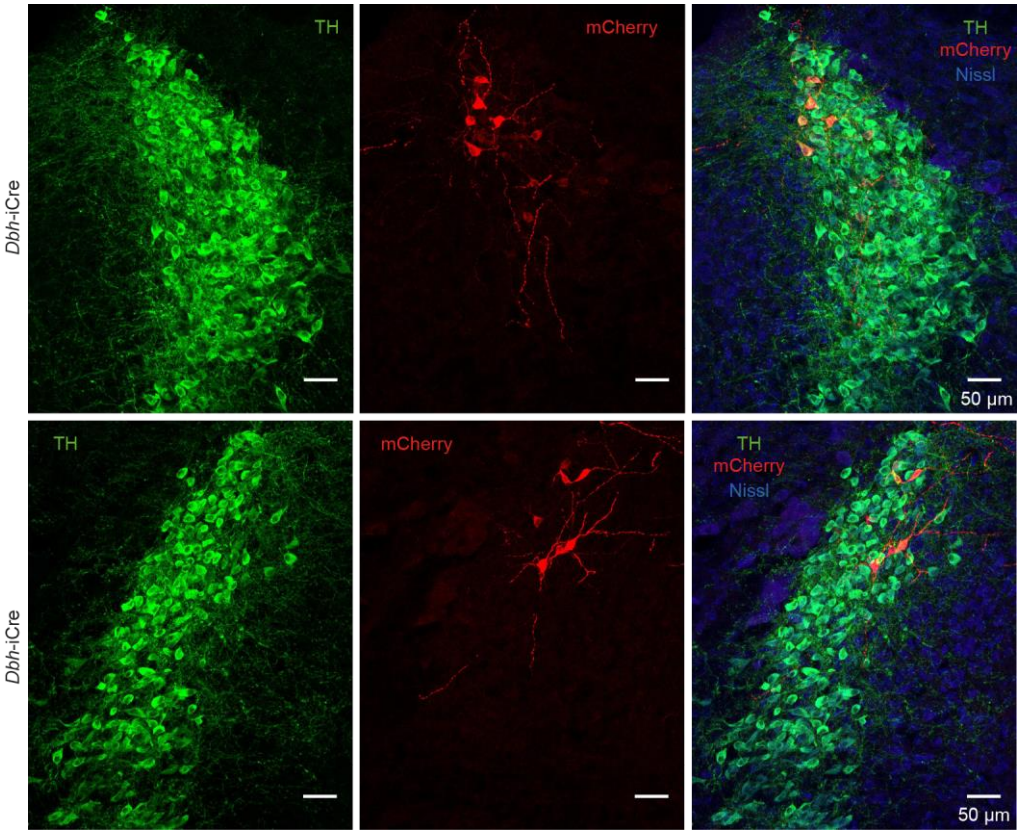

Figure S7. Related to Figure 7. Representative images from 2 DBH-iCre animals showing mCherry+ neurons in the LC after delivery of a Cre-dependent, mCherry-expressing retro-AAV2 in the dorsolateral caudate putamen.

Table S2. Related to Figure 4. Spearman's partial correlations considering multiple neuromodulatory receptor distributions. We calculated seven separate multiple regression models and determined Spearman's Rho (partial correlation) and associated P-value (FDR corrected) between the Node Modulation Index and the receptor distribution of interest after regressing out the contribution from all receptors belonging to a different neuromodulator family (i.e. adrenergic, dopaminergic, cholinergic nicotinic). Note that we did not partial out contributions from receptors within the same neuromodulator families due to their strong intrinsic co-expression. Significant correlations are indicated in bold.

Receptor distribution of interest	*Covariates of no interest*				
	Adrenergic	**Dopaminergic**	**Cholinergic**	**Spearman's Rho**	**p-value (FDR)**
Adrenergic Alpha-1		**x**	**x**	**0.2519**	**$4.11e^{-3}$**
Adrenergic Alpha-2		x	x	0.1269	0.1097
Adrenergic Beta-1		**x**	**x**	**0.2623**	**$7.75e^{-4}$**
Dopaminergic 1	**x**		**x**	**0.2005**	**0.0179**
Dopaminergic 4	**x**		**x**	**0.2219**	**0.0063**
Cholinergic Nicotinic Alpha-1	x	x		-0.011	0.8867
Cholinergic Nicotinic Gamma	x	x		0.030	0.7056